Extension of the Optimized Virtual Fields Method to estimate viscoelastic material parameters from 3D dynamic displacement fields

N. Connesson[a], E.H. Clayton[b], P.V. Bayly[b], F. Pierron[c]

[a] *Laboratoire TIMC-IMAG, Université de Grenoble (INPG-UJF), BP 53, 38041 Grenoble Cedex 9, France*
[b] *Department of Mechanical Engineering and Materials Science, Washington University in St. Louis, One Brookings Drive, Campus Box 1185, St. Louis, Missouri 63130, USA*
[c] *Engineering and the Environment, University of Southampton, Highfield, Southampton SO17 1BJ, UK*

Abstract

In-vivo measurement of the mechanical properties of soft tissues is essential to provide necessary data in biomechanics and medicine (early cancer diagnosis, study of traumatic brain injuries, *etc.*). Imaging techniques such as Magnetic Resonance Elastography (MRE) can provide 3D displacement maps in the bulk and in vivo, from which, using inverse methods, it is then possible to identify some mechanical parameters of the tissues (stiffness, damping etc.). The main difficulties in these inverse identification procedures consist in dealing with the pressure waves contained in the data and with the experimental noise perturbing the spatial derivatives required during the processing. The *Optimized* Virtual Fields Method (OVFM) [1], designed to be robust to noise, present natural and rigorous solution to deal with these problems. The OVFM has been adapted to identify material parameter maps from Magnetic Resonance Elastography (MRE) data consisting of 3-dimensional displacement fields in harmonically loaded soft materials. In this work, the method has been developed to identify elastic and viscoelastic models.

The OVFM sensitivity to spatial resolution and to noise has been studied by analyzing 3D analytically simulated displacement data. This study evaluates and describes the OVFM identification performances: different biases on the identified parameters are induced by the spatial resolution and experimental noise. The well-known identification problems in the case of quasi-incompressible materials also find a natural solution in the OVFM. Moreover, an *a posteriori* criterion to estimate the local identification quality is proposed. The identification results obtained on actual experiments are briefly presented.

Key words: MR elastography, elasticity reconstruction, inverse problem, virtual fields method, optimized virtual fields, noise sensitivity, noise robustness, elasticity, viscoelasticity

1. Introduction

The mechanical properties of tissues (stiffness, damping, *etc.*) are related to their compositions and structure. Mechanical property maps of organs can thus provide valuable information about locally abnormal tissues such as tumors [2, 3] without the need for invasive biopsies. Other applications concern the need to have representative material mechanical properties in order to simulate the response of biological tissues to shock, for instance to model the mechanics of traumatic brain injuries (TBI) [4–6]. The aim is thus usually to extract material parameter maps from *in vivo* and *ex vivo* data obtained in various organs: to study lungs [7], liver diseases [8, 9], muscle stiffnesses [10], brain properties [11–14], breasts tumours [15], blood vessel wall behaviour [16], skin [17] *etc.*

The identification of these mechanical properties is usually performed by analyzing 2D or 3D displacement field data which can be provided by different experimental techniques (Ultrasound [3], Optical Coherence Tomography [18], Magnetic Resonance Imaging (MRI) and Magnetic Resonance Elastography (MRE) [19, 20], *etc*). Depending on the measurement technique, different classes of mechanical excitation are used, including step compression, cyclic quasistatic compression, harmonic excitation, and transient excitation. The measured displacement fields contain information about the local mechanical properties of the tissues.

Many different analysis and post-processing methods have been developed to extract the material mechanical properties from full-field data. Two main inversion techniques are commonly used:

Email addresses: nathanael.connesson@gmail.com (N. Connesson), clayton@wustl.edu (E.H. Clayton), pvb@me.wustl.edu (P.V. Bayly), f.pierron@soton.ac.uk (F. Pierron)

Global inversion techniques: These identifications are usually based on Finite Element method. Local material parameters values are iteratively updated until the experimental displacement pattern is approximated by the simulation (finite element model updating [17], the constitutive equation gap method)

Local inversion techniques: These identification are based on the dynamic equilibrium equation governing the local displacement field. The main difficulties of these extractions consists in dealing properly with the material quasi-incompressibility and experimental noise:

- the quasi-incompressibility of biological materials induces ill-defined equation systems, or leads to the need for different assumptions to simplify the equilibrium equations [21]. It is thus often recommended to work with the curl of the displacement [21], adding an additional spatial derivative to the analysis. The method developed below does not require such additional spatial derivative yet naturally offers a rigorous way to deal with the material quasi-incompressibility.
- The estimation of the required spatial derivatives of the displacement field is prone to noise and alter parameter identification. The different proposed methods (review in [22], local frequency estimation or/and spatial Fourier transforms [7, 23], algebraic inversion of the differential equation [24], virtual fields method [16, 25], *etc.*) present different robustness to noise. Some of them have been specifically designed to better deal with low signal/noise ratio data by using, for example, spatial Fourier transform filtering [7].
  The aim of this work is to develop an alternative identification method based on the promising *optimized* virtual fields method presented initially in [1] and to test its noise filtering capabilities: the VFM proved indeed to be well adapted to analyze full-field measurement data and has already been used successfully to identify mechanical parameter maps in different experimental configurations (MRE (dynamic loading) [25, 26], MRI (static loading) [27], vibrating thin plates [28], *etc.*).

The data analyzed in this work are provided by MRE. The data are composed of 3-dimensional displacement fields measured at different times within the harmonic response of a harmonically loaded material (usually 4 to 8 frames over a period). In this work, the post-proccessing of the data is performed using the *optimized* virtual field method. In section 2, the *optimized* virtual fields method is first developed to locally identify an isotropic elastic model. The method is then extended to identify an isotropic viscoelastic model. The identification quality and sensitivity to different parameters is then analyzed on simulated data. A short study of actual experimental MRE data first provides information to simulate experimentally representative mechanical waves in elastic or viscoelastic materials (section 3). These analytical input data are then used to answer the following questions:

- What is the influence of spatial/temporal experimental data sampling ? (section 4.2)
- How does noise affect the identification? What is the method robustness? (section 4.3)

This work will help understand the *optimized* virtual fields method features and provide insight to make enlightened experimental and data processing choices. To the best of our knowledge, this study represents the first time that the *optimized* virtual fields method has been adapted to analyze 3D dynamic displacement fields, this is the first original contribution of the present paper. It is an essential step towards better elastography results with a view to evaluate the identification quality (uncertainty quantification), which is barely addressed in the literature. This is the second novelty of this article. Because of its simplicity and computational efficiency [29], we believe that the optimized VFM could lead to an automated identification tool to be diffused to the worldwide elastography community, with the potential to provide very fast ("nearly real time") identification.

2. Inversion problem

Let us consider a volume V of material harmonically loaded. The associated 3D displacement field $\overrightarrow{u}(x, y, z, t)$ at every point of the volume V is measured (spatial and temporal subsampling). This displacement field contains information about the material mechanical behaviour. The *optimized* virtual fields method, initially proposed in [1], can be developed in 3D and in dynamics to retrieve this information.

The local form of dynamic equilibrium in absence of body forces (and in small displacement hypothesis) can be written:

$$\overrightarrow{div}(\underline{\underline{\sigma}}) = \rho \frac{\partial^2 \overrightarrow{u}}{\partial t^2} \tag{1}$$

where $\underline{\underline{\sigma}}$ is the Cauchy stress tensor and ρ is the material density.

The principle of virtual work is obtained by multiplying the local equilibrium (equation 1) by a chosen virtual displacement field vector $\overrightarrow{u}^*$ and by integrating the obtained equation over a sub-volume V_m of the material. In this work, every variable related to the virtual fields will be denoted with a star such as X^*. The volume V_m has been chosen as a cube for the sake of simplicity but the following developments hold for any volume shape. In the case of small perturbations and in absence of body forces, the general expression of the principle of virtual work can be written as [29]:

$$\underbrace{-\int_{V_m} \underline{\underline{\sigma}} : \underline{\underline{\epsilon}}^* dV}_{Internal\ virtual\ work} + \underbrace{\int_{\partial V_m} \overrightarrow{T}.\overrightarrow{u}^* dS}_{External\ virtual\ work} = \underbrace{\int_{V_m} \rho \frac{\partial^2 \overrightarrow{u}}{\partial t^2}.\overrightarrow{u}^* dV}_{Acceleration\ virtual\ work} \tag{2}$$

where:

- ∂V_m is the boundary surface of the volume V_m,
- $\overrightarrow{T}$ is the stress vector (forces per unit area) on the boundary surface ∂V_m,
- $\underline{\underline{\sigma}}$ is the Cauchy stress tensor,
- $\overrightarrow{u}^*$ is a kinematically admissible **chosen** displacement field vector, referred to as "virtual displacement field",
- $\underline{\underline{\epsilon}}^*$ is the virtual strain tensor derived from $\overrightarrow{u}^*$ ($\underline{\underline{\epsilon}}^* = \frac{1}{2}(\underline{\underline{\text{grad}}}(\overrightarrow{u}^*) +^T \underline{\underline{\text{grad}}}(\overrightarrow{u}^*))$),
- ρ is the material density,
- ":" and "." are the dot products respectively between matrices and vectors.

The philosophy of the method consists in choosing the virtual displacement field $\overrightarrow{u}^*$ to enhance the required information while discarding unwanted data. For example, the stress vectors $\overrightarrow{T}$ acting over the boundary surface ∂V_m (local field of view) are definitely unknown in MRE data. It is thus chosen to nullify the external virtual work by imposing $\overrightarrow{u}^*(x, y, z) = 0$ over the boundary ∂V_m. With this virtual boundary condition, the principle of virtual work in equation 2 becomes [25]:

$$\underbrace{-\int_{V_m} \underline{\underline{\sigma}} : \underline{\underline{\epsilon}}^* dV}_{Internal\ virtual\ work} = \underbrace{\int_{V_m} \rho \frac{\partial^2 \overrightarrow{u}}{\partial t^2}.\overrightarrow{u}^* dV}_{Acceleration\ virtual\ work} \tag{3}$$

Contrary to usual quasi-statique VFM, it is the acceleration term that plays the role of a local "load-cell"' and contains the information. The dynamic loading is thus crucial for the success of the technique.

The material is supposed to be piecewisely homogeneous; equation 3 has been used to identify local material parameters over the sub-volume V_m, this volume being slid over the whole data volume V to obtain 3D maps of material parameters.

The principle of the virtual fields method is to substitute the stress tensor components in equation 3 using the constitutive equations (section 2.1). The continuous integrands are also approximated by discreet numerical integrations with the rectangle method. In elasticity, the equations are linear and selecting at least as many virtual fields as unknowns leads to a linear system containing the unknowns to identify (the material parameters). For most non-linear constitutive models, a set of non-linear equations is obtained that need to be solved with appropriate optimization algorithms [29]. In this work, the constitutive equations are linear and in this case, it was shown in [1] that for plane stress conditions, optimized virtual fields could be defined that lead to the maximum likelihood solution (minimal sensitivity to noise). The current work aims at extending this result to 3D dynamic data. The method is divided in two main steps: (1) choice of the virtual fields and (2) resolution of the linear system of equations. The following sections describe the material models used in the present study and then concentrate on the extension of optimized virtual fields in the case of 3D elasticity.

2.1. Material models

From an experimental point of view, stresses cannot be directly measured; the stress tensor $\underline{\underline{\sigma}}$ can only be related to the strain tensor $\underline{\underline{\epsilon}}$ through the definition of material models. In this work, the material models have been used both to simulate and identify different elastic and viscoelastic materials:

- Linear elastic material:

$$\underline{\underline{\sigma}} = K' \operatorname{Tr}(\underline{\underline{\epsilon}})\, \underline{\underline{I}} + 2G' \left[\underline{\underline{\epsilon}} - \frac{1}{3} \operatorname{Tr}(\underline{\underline{\epsilon}})\, \underline{\underline{I}} \right] \tag{4}$$

where K' is the bulk modulus and G' is the shear modulus. $\underline{\underline{I}}$ is the identity matrix and Tr is the trace operator. The bulk and shear moduli can be related to Young's modulus E' and Poisson's ratio ν by:

$$K' = \frac{E'}{3(1-2\nu)} \tag{5}$$

$$G' = \frac{E'}{2(1+\nu)} \tag{6}$$

With this material model and considering a harmonic loading of angular frequency ω, the mechanical response is also harmonic at the same angular frequency (linearity assumption). The principle of virtual work (equation 3) can be written as:

$$\left\langle \; f_K(\underline{\underline{\epsilon}}, \underline{\underline{\epsilon}}^*) \quad f_G(\underline{\underline{\epsilon}}, \underline{\underline{\epsilon}}^*) \; \right\rangle \begin{bmatrix} K' \\ G' \end{bmatrix} = \int_{V_m} \rho\omega^2 \overrightarrow{u} . \overrightarrow{u}^* dV \tag{7}$$

where

$$f_K(\underline{\underline{\epsilon}}, \underline{\underline{\epsilon}}^*) = \int_{V_m} \operatorname{Tr}(\underline{\underline{\epsilon}}) \operatorname{Tr}(\underline{\underline{\epsilon}}^*) dV \tag{8}$$

$$f_G(\underline{\underline{\epsilon}}, \underline{\underline{\epsilon}}^*) = \int_{V_m} 2\big(\underline{\underline{\epsilon}} : \underline{\underline{\epsilon}}^* - \frac{1}{3} \operatorname{Tr}(\underline{\underline{\epsilon}}) \operatorname{Tr}(\underline{\underline{\epsilon}}^*)\big) dV \tag{9}$$

The product $f_K(\underline{\underline{\epsilon}}, \underline{\underline{\epsilon}}^*)K'$ represents the virtual work due to the material volume variation (to bulk stresses); the product $f_G(\underline{\underline{\epsilon}}, \underline{\underline{\epsilon}}^*)G'$ represents the virtual work due to the shear stress.

For a better understanding of the OVFM features in the following developments, it will also prove useful to describe the actual material displacement field $\overrightarrow{u}$ as the sum of displacement fields due to bulk and shear waves ($\overrightarrow{u_K}$ and $\overrightarrow{u_G}$ respectively) so that $\overrightarrow{u} = \overrightarrow{u_K} + \overrightarrow{u_G}$. This additive decomposition is obtained by injecting the elastic model (equation 4) into the dynamic equilibrium equation (equation 1); $\overrightarrow{u_K}$ and $\overrightarrow{u_G}$ are respectively associated with the spherical and deviatoric part of the stress tensor. Applying the principle of virtual work to the definition of $\overrightarrow{u_K}$ and $\overrightarrow{u_G}$, two additional equations can be obtained:

$$f_K(\underline{\underline{\epsilon}}, \underline{\underline{\epsilon}}^*)K' = \int_{V_m} \rho\omega^2 \overrightarrow{u_K} . \overrightarrow{u}^* dV \tag{10}$$

$$f_G(\underline{\underline{\epsilon}}, \underline{\underline{\epsilon}}^*)G' = \int_{V_m} \rho\omega^2 \overrightarrow{u_G} . \overrightarrow{u}^* dV \tag{11}$$

which underlines that the virtual work due to the material volume variation $f_K(\underline{\underline{\epsilon}}, \underline{\underline{\epsilon}}^*)K'$ is related only to the virtual work of the bulk part $\overrightarrow{u_K}$ of the displacement field $\overrightarrow{u}$. The same conclusion holds for the shear part of the displacement field. As the bulk and pressure waves are intimately combined into the experimental data, the challenge consists in separating these two wave types from $\overrightarrow{u}$ to properly identify the material parameters K' and G'. This observation also holds for the viscoelastic model.

- Viscoelastic material:

The damping encountered in biological materials can be represented by a viscoelastic model [12–14] (dissipation proportional to the strain rate). Considering a harmonic loading of angular frequency ω, the strain-stress relation for such a viscoelastic material can be written as:

$$\begin{array}{rccccc} \underline{\underline{\sigma}} = & K' & \operatorname{Tr}(\underline{\underline{\epsilon}})\, \underline{\underline{I}} & + & 2G' & \left[\underline{\underline{\epsilon}} - \frac{1}{3} \operatorname{Tr}(\underline{\underline{\epsilon}})\, \underline{\underline{I}} \right] \\ & -\dfrac{K'\eta_K}{\omega} & \operatorname{Tr}\left(\dfrac{\partial \underline{\underline{\epsilon}}}{\partial t} \right) \underline{\underline{I}} & - & 2\dfrac{G'\eta_G}{\omega} & \left[\dfrac{\partial \underline{\underline{\epsilon}}}{\partial t} - \frac{1}{3} \operatorname{Tr}\left(\dfrac{\partial \underline{\underline{\epsilon}}}{\partial t} \right) \underline{\underline{I}} \right] \end{array} \tag{12}$$

where η_K and η_G are respectively the bulk and shear modulus loss factors.

To express the principle of virtual work (equation 3) with the viscoelastic model, the measured displacement field can be decomposed as the sum of two displacement field vectors in quadratic phase $\overrightarrow{u}_{\phi}$ and $\overrightarrow{u}_{\phi+\frac{\pi}{2}}$:

$$\overrightarrow{u} = \overrightarrow{u}_{\phi}\cos(\omega t) + \overrightarrow{u}_{\phi+\frac{\pi}{2}}\sin(\omega t) \tag{13}$$

Similarly, the strain tensor deriving from this displacement field vector ($\underline{\underline{\epsilon}} = \frac{1}{2}(\underline{\underline{\underline{\underline{\text{grad}}}}}(\overrightarrow{u}) + {}^{T}\underline{\underline{\underline{\underline{\text{grad}}}}}(\overrightarrow{u}))$ can be described as the sum of two strain tensors in quadratic phase:

$$\underline{\underline{\epsilon}} = \underline{\underline{\epsilon}}_{\phi}\cos(\omega t) + \underline{\underline{\epsilon}}_{\phi+\frac{\pi}{2}}\sin(\omega t) \tag{14}$$

Incorporating these definitions into the principle of virtual work (equation 3), and separating the terms in quadratic phases, a system of two equations can be written as follows:

$$\begin{bmatrix} \langle f_K(\underline{\underline{\epsilon}}_{\phi}, \underline{\underline{\epsilon}}^*) & f_G(\underline{\underline{\epsilon}}_{\phi}, \underline{\underline{\epsilon}}^*) & f_K(\underline{\underline{\epsilon}}_{\phi+\frac{\pi}{2}}, \underline{\underline{\epsilon}}^*) & f_G(\underline{\underline{\epsilon}}_{\phi+\frac{\pi}{2}}, \underline{\underline{\epsilon}}^*)\rangle \\ \langle f_K(\underline{\underline{\epsilon}}_{\phi+\frac{\pi}{2}}, \underline{\underline{\epsilon}}^*) & f_G(\underline{\underline{\epsilon}}_{\phi+\frac{\pi}{2}}, \underline{\underline{\epsilon}}^*) & -f_K(\underline{\underline{\epsilon}}_{\phi}, \underline{\underline{\epsilon}}^*) & -f_G(\underline{\underline{\epsilon}}_{\phi}, \underline{\underline{\epsilon}}^*)\rangle \end{bmatrix} \begin{bmatrix} K' \\ G' \\ K'' \\ G'' \end{bmatrix} = \begin{bmatrix} \int_{V_m} \rho\omega^2 \overrightarrow{u}_{\phi}.\overrightarrow{u}^* dV \\ \int_{V_m} \rho\omega^2 \overrightarrow{u}_{\phi+\frac{\pi}{2}}.\overrightarrow{u}^* dV \end{bmatrix} \tag{15}$$

where K'' and G'' are respectively the loss bulk and shear moduli ($K'' = -\eta_K K'$ and $G'' = -\eta_G G'$). Functions f_K and f_G (equations 8 and 9) are identical for both elastic and viscoelastic models.

This system is exactly identical to that usually obtained by directly injecting the complex notations $K = K' + iK''$ and $G = G' + iG''$ into the elastic model (equation 4) and considering complex displacement field vectors and strain tensors.

The 3D dynamic *optimized* virtual fields method is first developed to identify the elastic model parameters (equations 7, 8 and 9). The results are then extended to the viscoelastic model in section 2.7.

2.2. Special virtual fields

When an elastic model is identified, two material parameters (K' and G', equation 7) need to be determined. It is thus required to choose at least two independent virtual fields $\{\overrightarrow{u}^*_G, \underline{\underline{\epsilon}}^*_G\}$ and $\{\overrightarrow{u}^*_K, \underline{\underline{\epsilon}}^*_K\}$ among the infinity of possible virtual field vectors $\overrightarrow{u}^*$ and associated virtual strain tensors $\underline{\underline{\epsilon}}^*$. Yet, following the *optimized* virtual fields method [1], it is possible to choose a *special* virtual field $\{\overrightarrow{u}^*_G, \underline{\underline{\epsilon}}^*_G\}$ which dissociates the shear and bulk waves and is able to directly identify the shear modulus G'.

This property of the *special* virtual field is hereafter developed. Injecting the *special* virtual field $\{\overrightarrow{u}^*_G, \underline{\underline{\epsilon}}^*_G\}$ into equation 7, the principle of virtual work can be writen as:

$$K'\ f_K(\underline{\underline{\epsilon}}, \underline{\underline{\epsilon}}^*_G) + G'\ f_G(\underline{\underline{\epsilon}}, \underline{\underline{\epsilon}}^*_G) = \int_{V_m} \rho\omega^2 \overrightarrow{u}.\overrightarrow{u}^*_G\, dV \tag{16}$$

The *special* virtual field $\{\overrightarrow{u}^*_G, \underline{\underline{\epsilon}}^*_G\}$ is defined so as to simultaneously respect the two following conditions:

$$f_K(\underline{\underline{\epsilon}}, \underline{\underline{\epsilon}}^*_G) = 0 \tag{17}$$

$$f_G(\underline{\underline{\epsilon}}, \underline{\underline{\epsilon}}^*_G) = 1 \tag{18}$$

The choice of this virtual field will be referred to as step (1). Using those *special* virtual field properties, the material parameters can simply be computed during step (2) by simplifying equation 16 into:

$$G' = \int_{V_m} \rho\omega^2 \overrightarrow{u}.\overrightarrow{u}^*_G dV \tag{19}$$

The virtual field $\overrightarrow{u}^*_G$ directly extracts the shear modulus G' from the data; the identification of the shear modulus G' is independent of the identification of the bulk modulus K'.

To describe further how the specialization condition works, the condition $f_K(\underline{\underline{\epsilon}}, \underline{\underline{\epsilon}}^*_G) = 0$ (equation 17) associated to equation 10 can be written as:

$$K' f_K(\underline{\underline{\epsilon}}, \underline{\underline{\epsilon}}^*_G) = \int_{V_m} \rho\omega^2 \overrightarrow{u_K}.\overrightarrow{u}^*_G dV = 0 \tag{20}$$

The condition $f_K(\underline{\underline{\epsilon}}, \underline{\underline{\epsilon}}^*_G) = 0$ leads thus to choose a virtual field $\{\overrightarrow{u}^*_G, \underline{\underline{\epsilon}}^*_G\}$ which nullifies the acceleration virtual work of the bulk wave $\overrightarrow{u}_K$; the virtual field $\overrightarrow{u}^*_G$ selects only the shear wave data from $\overrightarrow{u}$ to compute the shear modulus G' (equation 19). Yet, the condition $f_K(\underline{\underline{\epsilon}}, \underline{\underline{\epsilon}}^*_G) = 0$ uses only the data contained into $\mathrm{Tr}(\epsilon)$ (equation 8) to define the virtual field $\underline{\underline{\epsilon}}^*_G$. For a quasi-incompressible material, $\mathrm{Tr}(\epsilon)$ is yet very small and noisy: in such case, this specialization condition does not contain enough information to efficiently nullify the acceleration virtual work of the bulk wave $\overrightarrow{u}_K$. Additional specialisation conditions will be proposed in this paper to better nullify the virtual work of the bulk wave (equation 20) when dealing with noisy data.

As the analyzed materials are quasi-incompressible in this work, the identified bulk modulus K' is expected to be erroneous due to low signal to noise ratio. For the sake of conciseness and due to the low identifiability of the bulk modulus K', only the virtual field $\{\overrightarrow{u}^*_G, \underline{\underline{\epsilon}}^*_G\}$ selected to identify the shear modulus G' has been developed in this paper.

At this point, two constraints have been applied to choose the virtual displacement fields during step (1): the virtual boundary condition $\overrightarrow{u}^*(x, y, z) = 0$ over the volume boundary ∂V_m and the specialization conditions expressed in equations 17 and 18. Yet, an infinite number of virtual fields can still be chosen. The idea consists then in selecting the virtual field $\{\overrightarrow{u}^*_G, \underline{\underline{\epsilon}}^*_G\}$ that minimize the effect of noise on the identified material parameters.

2.3. Noise effect

The displacement field injected into the virtual work equation is the **measured** discrete displacement field vector $\overrightarrow{u}^{exp}(x, y, z, t)$. This displacement field is modeled here as the sum of the actual displacement and a noise displacement field $\overrightarrow{u}^{no}$: $\overrightarrow{u}^{exp}(x, y, z, t) = \overrightarrow{u} + \overrightarrow{u}^{no}$ (noise sum model proposed in [1]). This noise in the displacement field implies a noise over the experimental strain tensor $\underline{\underline{\epsilon}}^{exp}$. Similarly, the experimental strain tensor $\underline{\underline{\epsilon}}^{exp}$ is modeled as the sum of the actual strain tensor $\underline{\underline{\epsilon}}$ and a noise strain tensor $\underline{\underline{\epsilon}}^{no}$: $\underline{\underline{\epsilon}}^{exp} = \underline{\underline{\epsilon}} + \underline{\underline{\epsilon}}^{no}$ where only $\underline{\underline{\epsilon}}^{exp}$ is guessed form the experimental data.

The experimental fields $\{\overrightarrow{u}^{exp}, \underline{\underline{\epsilon}}^{exp}\}$ are injected into equation 16. Due to the noise, the identified parameters are no longer the exact shear and bulk moduli G' and K' but approximated shear and bulk moduli G'_{app} and K'_{app}. Let's now analyze the error induced by the experimental noise. Using the linear properties of functions f_K and f_G (equations 8 and 9), the virtual work principle applied to noisy data (equation 16) can be written as:

$$K'_{app}\left((f_K(\underline{\underline{\epsilon}}, \underline{\underline{\epsilon}}^*_G) + f_K(\underline{\underline{\epsilon}}^{no}, \underline{\underline{\epsilon}}^*_G)\right) + G'_{app}\left(f_G(\underline{\underline{\epsilon}}, \underline{\underline{\epsilon}}^*_G) + f_G(\underline{\underline{\epsilon}}^{no}, \underline{\underline{\epsilon}}^*_G)\right) = \int_{V_m} \rho\omega^2 \overrightarrow{u}.\overrightarrow{u}^*_G \, dV + \int_{V_m} \rho\omega^2 \overrightarrow{u}^{no}.\overrightarrow{u}^*_G \, dV \tag{21}$$

The specialization conditions (equations 17 and 18) applied to the noisy signal are written:

$$f_K(\underline{\underline{\epsilon}}, \underline{\underline{\epsilon}}^*_G) + f_K(\underline{\underline{\epsilon}}^{no}, \underline{\underline{\epsilon}}^*_G) = 0 \tag{22}$$

$$f_G(\underline{\underline{\epsilon}}, \underline{\underline{\epsilon}}^*_G) + f_G(\underline{\underline{\epsilon}}^{no}, \underline{\underline{\epsilon}}^*_G) = 1 \tag{23}$$

Combining the specialization conditions (equations 22 and 23) with equation 21 and injecting the virtual work in noiseless conditions (equations 16), the identification errors $(G'_{app} - G')$ can be expressed independently from the measured strain field $\underline{\underline{\epsilon}}$:

$$(G'_{app} - G') = \underbrace{-K' \, f_K(\underline{\underline{\epsilon}}^{no}, \underline{\underline{\epsilon}}^*_G)}_{\substack{\text{virtual work} \\ \text{of the bulk wave strain noise}}} \quad \underbrace{-G' \, f_G(\underline{\underline{\epsilon}}^{no}, \underline{\underline{\epsilon}}^*_G)}_{\substack{\text{virtual work} \\ \text{of the shear wave strain noise}}} + \underbrace{\int_{V_m} \rho\omega^2 \overrightarrow{u}^{no}.\overrightarrow{u}^*_G \, dV}_{\text{virtual work of the acceleration noise}} \tag{24}$$

The identification error $(G'_{app} - G')$ is a linear combination of the virtual work of the bulk, shear and acceleration noises. It is worth noting at this point that this error equation holds for every **special** virtual field, whether this special virtual field is optimized or not (section 2.4). The aim is now to analyze the errors and thus define virtual field selection criteria so as to reduce the identification error.

- As expected, when the noise is zero ($\overrightarrow{u}^{no} = 0$ and $\underline{\underline{\epsilon}}^{no} = 0$), the internal virtual work of the noise is zero (equations 24, 8 and 9) and the shear modulus is perfectly identified independently on the chosen virtual field.
- When noise is in the signal, the different virtual works of the noise are not zero anymore:

– the virtual work of the acceleration noise $\int_{V_m} \rho\omega^2 \overrightarrow{u}^{no}.\overrightarrow{u}^*_G\, dV$ increases with the square of the loading angular frequency ω. Numerical tests with the parameters used in this work have shown this virtual work error to be negligible compared to both virtual works of the strain noise $-K' f_K(\underline{\underline{\epsilon}}^{no}, \underline{\underline{\epsilon}}^*_G)$ and $-G' f_G(\underline{\underline{\epsilon}}^{no}, \underline{\underline{\epsilon}}^*_G)$ (section 4.3): no additional criterion has thus been specified on $\overrightarrow{u}^*_G$ to reduce the virtual work of the acceleration noise $\int_{V_m} \rho\omega^2 \overrightarrow{u}^{no}.\overrightarrow{u}^*_G\, dV$.

– Theoretically, $f_K(\underline{\underline{\epsilon}}^{no}, \underline{\underline{\epsilon}}^*_G)$ and $f_G(\underline{\underline{\epsilon}}^{no}, \underline{\underline{\epsilon}}^*_G)$ are expected to be of identical order of magnitude (equations 8 and 9). Yet, as biological materials are quasi-incompressible, the bulk modulus K' is greater than the shear modulus G' (equations 5 and 6); the error induced by $K' f_K(\underline{\underline{\epsilon}}^{no}, \underline{\underline{\epsilon}}^*_G)$ is expected to be greater than the error induced by $G' f_G(\underline{\underline{\epsilon}}^{no}, \underline{\underline{\epsilon}}^*_G)$. Special attention is thus required to choose the virtual field $\overrightarrow{u}^*_G$ so as to enforce that the virtual work of the bulk wave strain noise $K' f_K(\underline{\underline{\epsilon}}^{no}, \underline{\underline{\epsilon}}^*_G)$ remains as close to zero as possible.

To design a proper selection criterion, the origin of the error $K' f_K(\underline{\underline{\epsilon}}^{no}, \underline{\underline{\epsilon}}^*_G)$ needs to be further analyzed: the specialization condition applied to noisy signal can be written $f_K(\underline{\underline{\epsilon}}, \underline{\underline{\epsilon}}^*_G) + f_K(\underline{\underline{\epsilon}}^{no}, \underline{\underline{\epsilon}}^*_G) = 0$ (equation 22). Considering equation 10, this condition implies that the virtual work of the bulk wave strain noise can be written:

$$K' f_K(\underline{\underline{\epsilon}}^{no}, \underline{\underline{\epsilon}}^*_G) = -K' f_K(\underline{\underline{\epsilon}}, \underline{\underline{\epsilon}}^*_G) = -\int_{V_m} \rho\omega^2 \overrightarrow{u_K}.\overrightarrow{u}^*_G dV \tag{25}$$

Due to the specialization condition, the virtual work of the bulk strain noise $K' f_K(\underline{\underline{\epsilon}}^{no}, \underline{\underline{\epsilon}}^*_G)$ is equal to the virtual work of the bulk wave $-\int_{V_m} \rho\omega^2 \overrightarrow{u_K}.\overrightarrow{u}^*_G dV$. Compared to the noiseless case (equation 20), the specialization of the virtual field in the noisy case does not anymore impose that the virtual field extracts only the virtual work of the shear wave from $\overrightarrow{u}$.

An additional condition can be devised to lower the noise impact by using the right part of equation 25: the virtual field $\{\overrightarrow{u}^*_G, \underline{\underline{\epsilon}}^*_G\}$ is chosen so that $\int_{V_m} \rho\omega^2 \overrightarrow{u_K}.\overrightarrow{u}^*_G dV = 0$. Such a condition would nullify the error coming from the virtual work of the bulk wave strain noise $K' f_K(\underline{\underline{\epsilon}}^{no}, \underline{\underline{\epsilon}}^*_G)$. By assuming that *(i)* the material density ρ is constant in V_m and *(ii)* the bulk wavelength λ_K is much greater than the integration volume V_m characteristic length, this additional condition is satisfied if:

$$\int_{V_m} u^*_{xG} dV = 0\ , \qquad \int_{V_m} u^*_{yG} dV = 0\ , \qquad \int_{V_m} u^*_{zG} dV = 0 \tag{26}$$

where u^*_{xG}, u^*_{yG}, and u^*_{zG} are the three components of the virtual displacement field $\overrightarrow{u}^*_G$.

It should be mentioned here that, at a loading frequency of 400 Hz,the pressure wave wavelength is about 3.7 m whereas the characteristic length of the integration volume V_m is lower than few millimeters in this work.

With this additional condition and considering that the virtual work of the acceleration noise is negligible, the identification error (equation 24) can be simply written:

$$(G'_{app} - G') = -G'\ f_G(\underline{\underline{\epsilon}}^{no}, \underline{\underline{\epsilon}}^*_G) \tag{27}$$

This analytical identification error will be numerically checked and validated in section 4.3.

- When the strain noise is much greater than the signal ($\underline{\underline{\epsilon}}^{no} \gg \underline{\underline{\epsilon}}$, *i.e.* $(\underline{\underline{\epsilon}} + \underline{\underline{\epsilon}}^{no}) \approx \underline{\underline{\epsilon}}^{no}$), the specialization conditions applied to the noisy signal (equations 22 and 23) are writen:

$$f_K(\underline{\underline{\epsilon}} + \underline{\underline{\epsilon}}^{no}, \underline{\underline{\epsilon}}^*_G) \approx f_K(\underline{\underline{\epsilon}}^{no}, \underline{\underline{\epsilon}}^*_G) = 0 \tag{28}$$

$$f_G(\underline{\underline{\epsilon}} + \underline{\underline{\epsilon}}^{no}, \underline{\underline{\epsilon}}^*_G) \approx f_G(\underline{\underline{\epsilon}}^{no}, \underline{\underline{\epsilon}}^*_G) = 1 \tag{29}$$

The identified shear modulus in extremely noisy data simply becomes (equations 24):

$$G'_{app} = \int_{V_m} \rho\omega^2 \overrightarrow{u}^{no}.\overrightarrow{u}^*_G\, dV \tag{30}$$

For extremely noisy signal, the specialization conditions thus leads to material parameters estimated equal to the virtual work of the acceleration noise, which will be shown to be very close to zero; these observations will be useful to analyze the results obtained in section 4.3.

2.4. Selecting an optimal virtual field

The idea developed in [1] is to use the error estimate to choose optimized virtual fields *i.e.* virtual fields reducing the error impact on the identification. This choice is still a part of step (1) and does not affect the equation solved during step (2). In this work, the virtual fields will be selected to minimize the identification error described in equation 27. As the virtual work of the acceleration noise has been neglected in this error expression, the selected virtual fields will not be perfectly optimized but will yet prove to provide very satisfactory results.

For different noise copies $\underline{\underline{\epsilon}}^{no}$, the identified parameter G'_{app} varies, thus creating a population of identified parameter. Using error expressed in equation 27, the mean identified parameter can be written:

$$E(G'_{app}) - G' = -G' \;\; E(f_G(\underline{\underline{\epsilon}}^{no}, \underline{\underline{\epsilon}}^{*}_{K})) \tag{31}$$

where $E(X)$ is the expectation of X.

The variance of the shear modulus can also be expressed:

$$V(G'_{app}) = E\big([G'_{app} - E(G'_{app})]^2\big) \tag{32}$$

To perform the analytical developments, the biases on the shear modulus distribution need to be neglected in equation 32: $[G'_{app} - E(G'_{app})] = [G'_{app} - G']$. According to equation 31, unbiased identified parameters can be obtained only if $E(f_G(\underline{\underline{\epsilon}}^{no}, \underline{\underline{\epsilon}}^{*})) = 0$. According to Wiener's theory [30], this occurs only if the strain noise $\underline{\underline{\epsilon}}^{no}$ and the virtual strain field $\underline{\underline{\epsilon}}^{*}$ are perfectly spatially uncorrelated. Due to the coupling between $\underline{\underline{\epsilon}}^{no}$ and $\underline{\underline{\epsilon}}^{*}$ expressed in the specialization conditions (equations 22 and 23) this condition can be approximately satisfied only for low noise levels. In the case of higher noise levels, the virtual fields selected by this method are thus not optimal anymore but yet provide robust identifications. With these hypotheses and injecting equation 27 into equation 32, the variance of the identified shear modulus population can be written as:

$$V(G'_{app}) \quad = G'^2 \quad E\big(f_G^2(\underline{\underline{\epsilon}}^{no}, \underline{\underline{\epsilon}}^{*}_{G})\big) \tag{33}$$

The variance of the shear modulus $V(G'_{app})$ depends on the strain noise $\underline{\underline{\epsilon}}^{no}$ and on the virtual strain fields $\underline{\underline{\epsilon}}^{*}_{G}$. In order to minimize the noise influence, the *special* virtual field $\{\overrightarrow{u}^{*}_{G}, \underline{\underline{\epsilon}}^{*}_{G}\}$ is chosen so as to minimize the variances $V(G'_{app})$ [1], which is equivalent to directly minimize the expectation $E\big(f_G^2(\underline{\underline{\epsilon}}^{no}, \underline{\underline{\epsilon}}^{*}_{G})\big)$. This *special* virtual field is referred to as *optimized* virtual field. A noise model must now be chosen to develop an automatic choice of the optimized virtual field.

2.5. Noise model

The noise in the strain tensor $\underline{\underline{\epsilon}}^{no}$ is directly related to the noise in the displacement field $\overrightarrow{u}^{no}$. In this work, the noise $\overrightarrow{u}^{no}$ at a specific time t is described using N_x, N_y and N_z, three independent copies of a standard centred Gaussian white noise on $\mathbb{R}^3$ (3 space dimensions). One can write:

$$\overrightarrow{u}^{exp} = \overrightarrow{u} + \overrightarrow{u}^{no} = \left\{ \begin{array}{c} U_x \\ U_y \\ U_z \end{array} \right\} + \gamma_u \left\{ \begin{array}{c} N_x \\ N_y \\ N_z \end{array} \right\} \tag{34}$$

where γ_u is the standard deviation of the displacement noise which is supposed to be identical over the three directions of space.

The strain tensor $\underline{\underline{\epsilon}}$ is computed by numerical centred differentiation at the time t from the experimental discrete displacement fields $\overrightarrow{u}^{exp}$. For example, $\epsilon_1 = \frac{\partial U_x}{\partial x}$ and $\epsilon_4 = \frac{\partial U_z}{\partial y} + \frac{\partial U_y}{\partial z}$ (Voigt notation). Considering the calculus rules for the sum of random variables, one can write:

$$\begin{array}{rclcl}
\epsilon_1^{exp} & = & \epsilon_1 + \gamma_{\epsilon 1} N_1 & = & \epsilon_1 + \dfrac{\gamma_u}{\sqrt{2}\Delta x} N_1 \\
\epsilon_2^{exp} & = & \epsilon_2 + \gamma_{\epsilon 2} N_2 & = & \epsilon_2 + \dfrac{\gamma_u}{\sqrt{2}\Delta y} N_2 \\
\epsilon_3^{exp} & = & \epsilon_3 + \gamma_{\epsilon 3} N_3 & = & \epsilon_3 + \dfrac{\gamma_u}{\sqrt{2}\Delta z} N_3 \\
\epsilon_4^{exp} & = & \epsilon_4 + \gamma_{\epsilon 4} N_4 & = & \epsilon_4 + \dfrac{\gamma_u}{\sqrt{2}} \sqrt{\dfrac{1}{\Delta y^2} + \dfrac{1}{\Delta z^2}}\, N_4 \\
\epsilon_5^{exp} & = & \epsilon_5 + \gamma_{\epsilon 5} N_5 & = & \epsilon_5 + \dfrac{\gamma_u}{\sqrt{2}} \sqrt{\dfrac{1}{\Delta x^2} + \dfrac{1}{\Delta z^2}}\, N_5 \\
\epsilon_6^{exp} & = & \epsilon_6 + \gamma_{\epsilon 6} N_6 & = & \epsilon_6 + \dfrac{\gamma_u}{\sqrt{2}} \sqrt{\dfrac{1}{\Delta x^2} + \dfrac{1}{\Delta y^2}}\, N_6
\end{array} \tag{35}$$

The ϵ_i^{exp} and ϵ_i strains respectively represent the strains computed from noisy and exact data. The N_i are six copies of a standard centred Gaussian noise. These noise copies are not perfectly independent from each other (6 noise copies related to N_x, N_y and N_z from the numerical differentiation in different directions) but will be considered as such in the following developments. The values $\gamma_{\epsilon i}$ represent the noise standard deviation over each strain component. Δx, Δy and Δz are the voxel lengths respectively in the $\overrightarrow{x}$, $\overrightarrow{y}$ and $\overrightarrow{z}$ directions.

The noise model proposed here allows to estimate the noise copies over the strain directly from the displacement noise, as in a real experiment. This model is slightly different from the noise model proposed in [1] where strain noise copies were directly added to the strain data. Computing the strain noises directly from the displacement noise also allows to deal with non cubic voxels ($\Delta x \neq \Delta y \neq \Delta z$) as is usually encountered in MRE measurements. The displacement field $\overrightarrow{u}$ could be spatially smoothed before computing the strain so as to reduce the noise level. Such a smoothing would alter the Gaussian nature of the noise and lead to non-*optimized* virtual fields selection. The same phenomena would also occur if the noise was not Gaussian. We have observed that the OVFM applied to non-Gaussian noise still provides excellent identification. The impact of smoothing and noise model is beyond the scope of the current paper and will be studied in future work.

The expectation $E(f_G(\underline{\underline{\epsilon}}^{no}, \underline{\underline{\epsilon}}^*_K))$ to be minimized can be expressed independently from the noise copies by using the properties of the Wiener integral of stochastic variables. If N_{f1} and N_{f2} are independent centered Gaussian noise copies and if f_1^* and f_2^* are spatial functions **independent from the noise copies**, Wiener's theory provides the expectations [30]:

$$E\left((\sum \gamma_1 N_{f1}\, f_1^* \Delta V)\,(\sum \gamma_1 N_{f1}\, f_2^* \Delta V)\right) = \gamma_1^2 (\sum f_1^* f_2^* \Delta V^2) \tag{36}$$

$$E\left((\sum \gamma_1 N_{f1}\, f_1^* \Delta V)\,(\sum \gamma_2 N_{f2}\, f_2^* \Delta V)\right) = 0 \tag{37}$$

To apply Wiener's theory to the expectation $E(f_G(\underline{\underline{\epsilon}}^{no}, \underline{\underline{\epsilon}}^*_K))$, the virtual fields ϵ_i^* (playing the role of functions f_1^* and f_2^* in equations 36 and 37) must thus be independent from the noise copies, which is not true in the general case due to the specialization conditions (equations 22 and 23). In this work, the Wiener's integrand properties have been applied considering small noise levels, *i.e.* when the specialization condition selects approximatively the same special virtual field for each noise copy. This condition is formally written [1]:

$$\gamma_{\epsilon i} \ll min(||\epsilon_j^*||) \tag{38}$$

With this hypothesis, using the definition of f_G (equations 9), approximating the continuous integrand with the rectangle method over the volume V_m and using the properties of Wiener's integrand, one obtains the following approximation:

$$E\big(f_G^2(\underline{\underline{\epsilon}}^{no}, \underline{\underline{\epsilon}}^*)\big) \approx \Delta V^2 \sum_{\text{voxels}\in V_m} \begin{pmatrix} 4\gamma_{\epsilon 1}^2 \left(\epsilon_1^* - \frac{1}{3}\,\mathrm{Tr}(\underline{\underline{\epsilon}}^*)\right)^2 \\ +4\gamma_{\epsilon 2}^2 \left(\epsilon_2^* - \frac{1}{3}\,\mathrm{Tr}(\underline{\underline{\epsilon}}^*)\right)^2 \\ +4\gamma_{\epsilon 3}^2 \left(\epsilon_3^* - \frac{1}{3}\,\mathrm{Tr}(\underline{\underline{\epsilon}}^*)\right)^2 \\ +\gamma_{\epsilon 4}^2 \epsilon_4^{*2} + \gamma_{\epsilon 5}^2 \epsilon_5^{*2} + \gamma_{\epsilon 6}^2 \epsilon_6^{*2} \end{pmatrix} \tag{39}$$

where $\Delta V = \Delta x \Delta y \Delta z$ is a voxel volume. More details on the calculations can be found in [29] for the plane stress case.

As this function is independent from the strain tensor specific noise copies $\underline{\underline{\epsilon}}^{no}$, it can directly be used to define the *optimized* virtual displacement fields minimizing the shear modulus variance for a single random noise copy. The variance being quadratic in the virtual fields components, this minimum is unique.

2.6. Virtual field function basis and optimized virtual fields

At this point, the 3D virtual displacement fields ($\overrightarrow{u}^*$, $\underline{\underline{\epsilon}}^*$) can be described using any basis of C^o functions (4^{th} order polynomials [25], harmonic functions [26], piecewise polynomials [31], *etc.*). In this work, the 3D virtual displacement field vectors $\overrightarrow{u}^*(x,y,z)$ have been defined using **piecewise** functions (8-noded finite element bricks [31]): the virtual displacement field on the volume V_m is described by sub-domains. It has been chosen here to juxtapose 4^*x4^*x4^* virtual elements, thus creating a macro-element composed of 64 brick elements and 125 nodes (Figure 1c, properties sumarized in Table 3, line 1). Effect of the virtual field richness will shortly be studied in section 4.3.

A local identification of the material parameters is performed over this macro-element. Each node i has 3 degrees of freedom ($q_x^{i*}, q_y^{i*}, q_z^{i*}$). The nodal displacements of the entire macro-element will be denoted ($\{q_x\}^{(m*)}, \{q_y\}^{(m*)}, \{q_z\}^{(m*)}$)

and can be organized as a column vector:

$$\{q^{m*}\} = \left\{ \begin{array}{c} \{q_x\}^{(m*)} \\ \{q_y\}^{(m*)} \\ \{q_z\}^{(m*)} \end{array} \right\} \tag{40}$$

The macro-element contains 125 nodes; the macro-element nodal displacement vector $\{q^{m*}\}$ contains 3x125 = 375 rows.

With this virtual field function basis, the virtual field chosen on V_m depends only on the macro-element nodal virtual displacements $\{q^{m*}\}$. The macro-element nodal virtual displacement $\{q_G^{m*}\}$ associated with the virtual field $\{\overrightarrow{u}^*_G, \underline{\underline{\epsilon}}^*_G\}$ is chosen during step (1) so as to:

1. respect the virtual boundary condition $\overrightarrow{u}^*(x,y,z) = 0$ on the volume boundary ∂V_m,
2. satisfy the specialization conditions (equations 17 and 18) and the additional condition (equation 26),
3. and minimize the variance $V(G')$ by minimizing the function $E\big(f_G^2(\underline{\underline{\epsilon}}^{no}, \underline{\underline{\epsilon}}^*_G)\big)$ (equations 33 and 39) .

From a mathematical point of view, all these conditions can be written as relations on the macro-element nodal virtual displacements $\{q_G^{m*}\}$.

1. *Boundary conditions:* the nodal displacements of all nodes of the macro-element located on the volume boundary ∂V_m are assigned to be zero. For a 4*x4*x4* macro-element, these boundary conditions imply that 98 nodes over 125 are blocked, leaving 27 free nodes. These constraints can be written as linear relationship on $\{q_G^{m*}\}$:

$$[A_{CL}]\{q_G^{m*}\} = \{0\} \tag{41}$$

   where $[A_{CL}]$ is a 98 rows by 375 column matrix.

2. *Specialization and additional conditions:* by using the shape functions on each element and combining them on the macro-element, the functions $f_K(\underline{\underline{\epsilon}}, \underline{\underline{\epsilon}}^*_G)$ and $f_G(\underline{\underline{\epsilon}}, \underline{\underline{\epsilon}}^*_G)$ (equations 8 and 9) and integrand taking part in the additional condition can be approximated by using rectangle integration on each voxel and expressed directly as a function of $\{q_G^{m*}\}$:

$$f_K(\underline{\underline{\epsilon}}, \underline{\underline{\epsilon}}^*_G) = \langle A_K \rangle \{q_G^{m*}\} \quad \text{and} \quad f_G(\underline{\underline{\epsilon}}, \underline{\underline{\epsilon}}^*_G) = \langle A_G \rangle \{q_G^{m*}\} \tag{42}$$

$$\left[\begin{array}{c} \int_{V_m} u^*_{xG} dV \\ \int_{V_m} u^*_{yG} dV \\ \int_{V_m} u^*_{zG} dV \end{array} \right] = \left[\begin{array}{c} \\ [A_{RB}] \\ \\ \end{array} \right] \{q_G^{m*}\} \tag{43}$$

   where $[A_{RB}]$, $\langle A_K \rangle$ and $\langle A_G \rangle$ are respectively a matrix and vectors containing 375 columns. The vectors $\langle A_K \rangle$ and $\langle A_G \rangle$ are thus built up using the experimental data, the chosen virtual field basis definition and the chosen material model. Matrix $[A_{RB}]$ is independent of experimental data. With this notation, the additional and specialization conditions (equations 22, 23 and 26) leading to the special virtual field $\{\overrightarrow{u}^*_G, \underline{\underline{\epsilon}}^*_G, q_G^{m*}\}$ are simply written as:

$$\left[\begin{array}{c} \int_{V_m} u^*_{xG} dV \\ \int_{V_m} u^*_{yG} dV \\ \int_{V_m} u^*_{zG} dV \\ f_K(\underline{\underline{\epsilon}}, \underline{\underline{\epsilon}}^*_G) \\ f_G(\underline{\underline{\epsilon}}, \underline{\underline{\epsilon}}^*_G) \end{array} \right] = \left[\begin{array}{c} [A_{RB}] \\ \langle A_K \rangle \\ \langle A_G \rangle \end{array} \right] \{q_G^{m*}\} = \left\{ \begin{array}{c} \left\{ \begin{array}{c} 0 \\ 0 \\ 0 \end{array} \right\} \\ \langle\ 0\ \rangle \\ \langle\ 1\ \rangle \end{array} \right\} \tag{44}$$

3. *Variance minimization:* the *special* virtual nodal displacements $\{q_G^{m*}\}$ must also be chosen to minimize the quadratic function $E\big(f_G^2(\underline{\underline{\epsilon}}^{no}, \underline{\underline{\epsilon}}^*_G)\big)$ (equation 39), which can be written as a function of $\{q_G^{m*}\}$: using the shape functions of each element and combining them over the macro-element, one can write:

$$E\big(f_G^2(\underline{\underline{\epsilon}}^{no}, \underline{\underline{\epsilon}}^*_G)\big) = \frac{\gamma_u^2}{2} \{q_G^{m*}\}^T [H_G] \{q_G^{m*}\} = \gamma_u^2 \eta_G^2 \tag{45}$$

   where $[H_G]$ is a semi-definite positive symmetric square matrix [1]. $\{q_G^{m*}\}^T$ is the transpose of vector $\{q_G^{m*}\}$. It should also be pointed out that matrix $[H_G]$ is dependent on the chosen material model and basis of functions but is independent from the deformation data.

The goal is then to choose the virtual nodal displacements $\{q_G^{m*}\}$ minimizing the variance (equation 45) while respecting the constraints expressed in equations 41 and 44. The virtual nodal displacement vector $\{q_G^{m*}\}$ is in fact the saddle point of the Lagrangian $\mathcal{L}_G$ written [1]:

$$\mathcal{L}_G = \frac{\gamma_u^2}{2}\{q^{m*}\}^T[H_G]\{q^{m*}\} + \{\Lambda_G\}^T([A]\{q^{m*}\} - \{Z_G\}) \tag{46}$$

where $\{\Lambda_G\}$ is the vector composed of the Lagrangian multipliers, $[A]$ is the constraint matrix given by:

$$[A] = \begin{bmatrix} [A_{CL}] \\ [A_{RB}] \\ \langle A_K \rangle \\ \langle A_G \rangle \end{bmatrix} \tag{47}$$

and

$$\{Z_G\} = \begin{Bmatrix} \{0\} \\ \{0\} \\ \begin{Bmatrix} 0 \\ 1 \end{Bmatrix} \end{Bmatrix} \tag{48}$$

Vector $\{q_G^{m*}\}$ at the saddle point of the Lagrangian $\mathcal{L}_G$ respects the condition:

$$[A]\{q_G^{m*}\} = \{Z_G\} \tag{49}$$

From a practical point of view, the saddle point $\{q_G^{m*}\}$ of the Lagrangian $\mathcal{L}_G$ can be obtained simply by solving the following linear system:

$$\left[\begin{array}{c|c} [H_G] & [A]^T \\ \hline [A] & [0] \end{array}\right] \begin{Bmatrix} \{q_G^{m*}\} \\ \{\Lambda_G\} \end{Bmatrix} = \{Z_G\} \tag{50}$$

Once the *optimized* virtual node displacements $\{q_G^{m*}\}$ have been chosen to reduce the noise effect (step (1)), a the shear modulus G'_{app} is estimated using equation 19 (step (2)). No iterative process is required here since minimizing the shear modulus variance is equivalent to minimize the expectation $E\big(f_G^2(\underline{\underline{\epsilon}}^{no}, \underline{\underline{\epsilon}}_G^*)\big)$ (equation 33), which is independent of the identified material parameters.

The application and performances of this identification method are illustrated using simulated data in section 3 and 4. In the next section, we describe how the optimized virtual fields method may be developed to identify the viscoelastic models.

2.7. Viscoelastic model identification

The reasonings are similar for the elastic and viscoelastic models, simply changing the initial expression of the virtual work (elastic: equation 7, viscoelastic: equation 15). The viscoelastic model involves four parameters K', K'', G' and G'' (equation 12). As the principle of virtual work applied to the viscoelastic model provides a system of two equations (equation 15), two virtual fields would be required to estimate the four parameters. Yet, using the properties of *special* virtual fields, the shear storage and loss moduli G' and G'' have been identified using a single *special* virtual field $\{\overrightarrow{u}_G^*, \underline{\underline{\epsilon}}_G^*\}$. One virtual field is enough to identify the two parameters since the spatial information relates to G' (and are affected by the choice of the virtual fields) whereas the information about the split between storage and loss moduli G'' is contained in the temporal measurements. This was already seen in [32].

The analytical expression of the specialization conditions, the final system and errors have been reported in appendix for the sake of conciseness. The parameter variances $V(X_{app})$ have been analytically developed by supposing that the noises $\underline{\underline{\epsilon}}_\phi^{no}$ and $\underline{\underline{\epsilon}}_{\phi+\frac{\pi}{2}}^{no}$ were spatially independent and of the same amplitude ($\gamma_{\epsilon_\phi i} = \gamma_{\epsilon_{\phi+\frac{\pi}{2}} i}$). This noise independence has been numerically checked. With this hypothesis and using the equations developed in appendix, the final expressions $V(G'_{app})$ and $V(G''_{app})$ are simply written as:

$$V(G'_{app}) = V(G''_{app}) = \frac{1}{2}(G'^2 + G''^2)\ E\big(f_G^2(\underline{\underline{\epsilon}}_\phi^{no}, \underline{\underline{\epsilon}}_G^*)\big) \tag{51}$$

where the function $E(f_G^2)$ is similar to the function defined for the elastic material (equation 39). As for the elastic case, the virtual field is chosen so as to minimize the expectation $E(f_G^2)$.

It should be underlined here that the variance on the shear and loss moduli G' and G'' are equal; the relative error on the loss shear modulus G'' will be bigger than on the storage shear modulus G' since it is expected to observe $G'' < G'$.

Now that the *optimized* virtual fields method has been developed, the objective is first to validate the equations on simulated data and evaluate the performance of the method.

3. Input data: 3D displacement fields

In order to validate the proposed equations and analyze the performances of the *optimized* virtual fields method, analytical displacement fields have been simulated. Many different parameters may impact the identification quality. Some parameters are related to the input data such as the wavelengths of the mechanical waves λ_K and λ_G, the spatial resolution, the local signal to noise ratio of the measurements, *etc.* Some other parameters are directly related to the identification such as the size of the macro-element, the number of finite elements composing the macro-element, the ability of the chosen material model to describe the actual material behaviour, *etc.* Understanding the effect of each parameter on the identification is essential to assess the quality of the identification and its robustness, as well as to provide guidelines to the selection of the different parameters of the procedure (size of the macro element, smoothing etc.). In this study, it has been chosen to study specifically the bias and error associated to two main parameters:

- the spatial resolution (data sampling) (section 4.2),
- the local signal to noise ratio (section 4.3).

The characteristics of the simulated analytical displacement fields and the associated noise levels have been chosen in reference to some experimental 3D displacement fields.

3.1. Experimental data

The experimental data taken for reference in this work have been obtained on a 20x20x20 mm^3 cubic gel sample (Figure 1) [26]. During this experiment, a harmonic shear load has been applied to one of the cube surfaces (normal $\overrightarrow{y}$, surface displacement in direction $\overrightarrow{x}$) at a frequency of $f = 400$ Hz. Eight 3D displacement fields $\overrightarrow{u}(x, y, z, t)$ shifted by a constant period fraction have been acquired using an MRE encoding sequence (sampling of $f_s = 8f$). The experimental voxel sizes are of Δx x Δy x $\Delta z = 0.25$ x 0.25 x 0.5 mm^3.

The first harmonic of the displacement field has been extracted from the data using a temporal Fourier analysis. Such a Fourier analysis provides 3D amplitude and phase maps (respectively $\overrightarrow{M}^{400}(x, y, z)$ and $\overrightarrow{\phi}^{400}(x, y, z)$) such that:

$$\overrightarrow{u}^{400}(x, y, z, t) = \begin{pmatrix} U_x^{400}(x, y, z, t) \\ U_y^{400}(x, y, z, t) \\ U_z^{400}(x, y, z, t) \end{pmatrix} = \overrightarrow{M}^{400}(x, y, z) cos(\omega t + \overrightarrow{\phi}^{400}(x, y, z) + \overrightarrow{\phi}_0) \tag{52}$$

The phase $\overrightarrow{\phi}_0$ represents the unknown initial phase shift associated with the time reference $t = 0$ chosen arbitrarily during the experiment. It underlines thus that the mean value of the phase map $\phi^{400}(x, y, z)$ is unknown due to experimental constraints. This unknown will prove to affect the identification performances. The superscript X^{400} underlines that the considered value is provided by the harmonic $f = 400$ Hz extracted from the Fourier analysis.

The displacement components U_x^{400}, U_y^{400} and U_z^{400} along line Δ (defined in Figure 1) are plotted in Figure 2: a loading displacement amplitude of 40 μm peak to peak is applied at coordinate $y = 0$ in the $\overrightarrow{x}$ direction; the displacement amplitudes U_x^{400} are thus one order of magnitude larger than U_y^{400} and U_z^{400}.

Close to the loading point ($y = 0$), the waves are traveling in the $\overrightarrow{y}$ direction and their amplitude decreases due to the material damping. When the traveling shear waves encounters the cube boundary ($y = 20$ mm), part of the waves is reflected (hard boundary condition). The superposition of the incoming and reflected waves creates local standing waves characterized by the presence of nodes (spatial localization where the displacement amplitude envelopes $|\overrightarrow{M}^{400}(x, y, z)|$ are close to zero).

Due to the loading conditions, the experimental displacement field probably also contains pressure waves of small amplitude traveling in the $\overrightarrow{x}$ direction. Such waves that can not be easily observed directly from the experimental field.

3.2. Analytical data +"experimental" noise

In order to precisely evaluate the identification performances, analytically simulated displacement fields have been used: the material input properties are chosen and used as reference (Table 1). For the sake of conciseness, the analytical solutions of the pressure and shear waves have been reported in appendix. The analytical wave equations have been spatially and temporally sampled: the averaged displacement over each voxel is computed so as to mimic actual measurement recording. As for the experimental data, the analytical displacement fields are composed of:

(i) a plane shear wave traveling in the $\overrightarrow{y}$ direction (loading in the $\overrightarrow{x}$ direction, shear wave amplitude $U_{Sx}(y = 0) = 20\mu m$), and

(ii) a plane pressure wave traveling in the $\overrightarrow{x}$ direction (pressure wave amplitude $U_{Kx}(y=0) = 1\mu m$).

The identification performances have been studied with (a) soft boundary conditions (waves traveling in infinite medium), or with (b) hard boundary conditions at $y = 20\ mm$ (Figure 3). One can observe how the figures mimic the waves previously observed in the gel cube experiment (Figure 2a). As in the experimental data, the presence of pressure wave in the data is almost unnoticeable (pressure wave amplitude of 2 μm peak to peak versus shear wave amplitude of 40 μm).

A standard centred Gaussian noise of standard deviation γ_u has been added to each frame of the data, which results into a noise of standard deviation γ_u^{400} after the Fourier analysis. The noise amplitude γ_u^{400} has been estimated to be of $\gamma_u^{400} = 0.04\ \mu m$ from the experimental data (0.2% of the loading amplitude). In more standard in-vivo clinical measurements, the noise level is expected to be higher. Noise levels γ_u^{400}/U_x^{400} up to 3% have thus also been studied.

Even if the basic hypothesis in the optimized virtual fields is that the noise amplitude remains small compared to the signal, we show that selected virtual fields are excellent.

4. Results and discussion

We apply the virtual fields method locally so as to identify local material parameter: the macro-element of volume V_m is moved voxel by voxel over the 3D frame at a specific time t (equation 3, Figure 1c). The local displacement amplitude changes during a loading period (Figures 2 and 3). The signal to noise ratio is thus both space and time dependent; the local identified material parameters shall be different depending on the analyzed time t. To take this space-time dependence into account, a set of material parameters is identified at each spatial position and at different times during the loading cycle. Space-time material parameter maps are thus constructed. It has been chosen in this work to identify 50 sets of material parameters over one cycle ($\omega t = 2\pi n/50$ with n an integer such as $n \in [0, 49]$). As the input data is only composed of 8 frames shifted over a cycle, the required displacement fields at the different times t are interpolated using the first displacement harmonic extracted thanks to the temporal Fourier transform (equation 52).

From a general point of view, an analysis is composed of the following steps.

1. Independent Gaussian noise copies are added to each displacement frame.
2. The first displacement harmonic is extracted from the input data using a temporal Fourier transform.
3. The 3D displacement field is interpolated at a $t = t_i$ (frame i).
4. If required, frame i is spatially smoothed using a Gaussian filter to lower the high frequency noise level.
5. A material parameter map at a time t_i is computed from frame i using the *optimized* virtual fields method.
6. Back to step 3: the 3D displacement field is interpolated at $t = t_{i+1}$ (frame $i + 1$), *etc.*

The theory providing optimized virtual fields have been first checked in section 4.1. Then, the influence of the spatial resolution (data sampling, section 4.2), local signal to noise ratio and and virtual field richness (section 4.3) has been studied. The method is then applied to the presented experimental data.

4.1. Theory validation

As a first step, the variance formulation (equations 33, 51) used to select the optimized virtual fields has been checked using the method proposed in [1]. According to equation 45, the experimental variances of the identified parameter distribution $V(X'_{app})$ should be linear with γ_u^2 and of slope η_X^2. The theory can thus be checked by verifying that the experimental variance is linear with γ_u^2, *i.e.* $V(X'_{app}) = \eta_X^{exp\,2}\gamma_u^2$, and that its slope $\eta_X^{exp\,2}$ is equal to the slope predicted by the theory η_X^2.

For the elastic model, a population of identified parameters G'_{app} has been computed for 30 different noise levels γ_u and for 30 different noise copies for each noise level. All parameters have been identified at the same time t and same spatial position. The experimental coefficient of variation $\frac{\sqrt{V(G'_{app})}}{G'}$ has been reported versus the relative noise level $\frac{\gamma_u^{400}}{U_{x0}}$ in Figure 4. Two cases have been studied:

- First, the noise $\underline{\underline{\epsilon}}^{no}$ on the strain fields have been introduced using 6 independent Gaussian noise copies [1]. The standard deviations of these noises is related to the standard deviation of the displacement noise by equation 35. In this case (empty markers, dashed lines), the experimental values η_X^{exp} are equal to the theoretical values η_X, proving the consistency of the developed approach.

- Subsequently, the noise $\underline{\underline{\epsilon}}^{no}$ on the strain fields has been computed after adding the noise fields N_x, N_y and N_z to the displacement, as for a real experiment. In this case (full markers, continuous lines), the experimental linear coefficients η_X^{exp} are lower than the theoretical coefficient η_X. This behaviour underlines a correlation at a low level between the strain noise fields (3 noise copies on the displacement fields provide 6 noise copies on the strain fields $\underline{\underline{\epsilon}}^{no}$). As the experimental values η_X^{exp} are lower than the theoretical values η_X, the noise correlation improves the variance minimization. It has been supposed that this correlation between the strain field noises only has a limited impact on the optimized virtual field choice.

The same behaviour has been observed for the viscoelastic model.

4.2. Bias induced by the spatial resolution

The first bias studied is this work is directly associated to the experimental parameters: the measured displacement data are discrete; the mechanical waves are temporally and spatially sampled. The question that arises is that of the influence of the spatial data sampling on the identified parameters. This issue has been studied by using different spatial resolutions of the analytical models. The effect of these different spatial resolutions has been studied in the following cases:

i. Elastic model identified from elastic traveling waves.
ii. Elastic model identified from elastic standing waves.
iii. Viscoelastic model identified from viscoelastic waves.

In these analytical cases, the reference and identified material models are matching in order to separate the sources of bias. As a consequence, the identified parameters are the same regardless of time and space and the results can be represented with a single value for each spatial resolution. An example of pressure and shear elastic standing waves (case ii.) obtained with a data sampling of 7 voxels per shear wavelength λ_G is presented in the right-hand side of Figure 5. The relative error on the shear modulus G' are presented in Figure 5.

The different studied cases provide similar results: the relative errors are superimposed and converge towards zero when the spatial resolution increases. The relative errors on the loss modulus G'' identified using the viscoelastic material (not plotted) present similar behaviour but are lower than 1.5% for a spatial resolution of 3 voxels per shear wavelength only. This is consistent with the fact that the loss moduli information is mainly contained into the wave phase-shift.

It has also been checked that these results hold for different macro-element sizes and element numbers provided that **linear** virtual elements are used and no noise is added to the analytical models.

In the following analyses, a spatial resolution of 16 voxels per shear wavelength λ_G was used. This resolution has been chosen as it is representative of the experimental data obtained from the cubic gel sample (Figure 2). The chosen 8x8x8 voxels macro-element thus contains half a shear wavelength $\lambda_G/2$ ($V_m = (\lambda_G/2)^3$, Figure 1). These parameters lead to overestimate G' by 1.3% in noiseless conditions (Figure 5). The loss modulus G'' is underestimated by $1.5.10^{-3}$%. The material parameters identified in these conditions will be used as references in the rest of this work and will be denoted respectively G'_{ref} and G''_{ref}. The influence of the other parameters such as noise is studied hereafter.

4.3. Noise robustness

The experimental noise induces uncertainties in the identified parameters. The task is to evaluate the effect of this noise on the identification. To our knowledge, few systematic studies of inversion robustness to noise (such as that in [24]) are available in the literature. In this work, the OVFM ability to deal with noise in quasi-incompressible materials has been studied on the noisy analytical waves previously presented in Section 3.2 (Figure 3).

As in the experimental data, a centered Gaussian noise of standard deviation $\gamma_u^{400} = 0.04$ μm (0.2% of the loading amplitude) is added to the analytical displacement field (Figure 6a). **In this case, the U_y^{400} and U_z^{400} displacement fields contain only noise wherease the U_x^{400} fields contains noisy shear and pressure waves.** The shear storage and loss moduli G'_{app} and G''_{app} have been identified by moving the mobile windows along axis $\overrightarrow{y}$ and for 40 time steps over a period.

Storage shear modulus G'_{app}: The storage shear modulus relative error map ($\frac{G'_{app}-G'_{ref}}{G'_{ref}}$) is presented in Figure 6b. As expected, the space-phase map shows that the identified shear modulus depends both on time and space. To better understand the identification time dependency, let's consider the specific time t_c when the center (x_c, y_c, z_c) of the volume V_m is located at a point where the displacement is zero ($\overrightarrow{u}(x_c, y_c, z_c, t_c) = 0$). In this

case, the experimental displacement field $\overrightarrow{u}$ is maximal on some boundaries of the volume V_m due to the macro-element size ($V_m = (\lambda_G/2)^3$). Yet, the virtual displacement field $\overrightarrow{u}^*_G$ is set equal to zero on the boundaries ($\overrightarrow{u}^*(\partial V_m) = 0$). **Since the shear modulus is computed by $G' = \int_{V_m} \rho\omega^2 \overrightarrow{u}.\overrightarrow{u}^*_G dV$ (when identifying an elastic model, equation 19), most of the signal in $\overrightarrow{u}$ is thus discarded while computing the product $\overrightarrow{u}.\overrightarrow{u}^*_G$ at the specific time** t_c; the virtual field vector amplitude of $\overrightarrow{u}^*_G$ must be artificially increased so that the integrand reaches G'. From a mathematical point of view, this artificial increase is performed while applying the specialization condition $f_G(\underline{\underline{\epsilon}}, \underline{\underline{\epsilon}}^*_G) = 1$ (equation 18).

On the contrary, good local signal to noise ratio will be obtained when the required virtual field vector amplitude of $\overrightarrow{u}^*_G$ is relatively small, *i.e.* when the signal is naturally contained in $\overrightarrow{u}$ rather than artificially increased by $\overrightarrow{u}^*_G$ when computing the integrand $G' = \int_{V_m} \rho\omega^2 \overrightarrow{u}.\overrightarrow{u}^*_G dV$. The best identified shear modulus G' over time t_c should thus be obtained with the optimized virtual fields requiring the minimal amplitude $|\{q^{m*}_G\}|$. This is confirmed by the place of diamonds in Figure 6b which are localized at times when the identification errors are close to zero. The shear moduli identified with the optimized virtual fields requiring the minimal amplitude $|\{q^{m*}_G\}|$ will be referred as G'_{best} and G''_{best}.

The time-space map has been summarized in Figure 6c:

- The vertical black line represents the shear modulus G'_{ref} identified from noiseless data.
- The maximal and minimal identified shear modulus G'_{app} versus time (respectively circles and squares), denoted respectively $max(G', t)$ and $min(G', t)$, provide insight about the local identification time dependency and identification quality: as the signal amplitude decreases due to the material damping, the identification time dependency increases and a bias appears on the identified modulus. The identified shear moduli G' are thus globally underestimated which is a consequence of the specialization condition applied to noisy data: as the signal to noise ratio worsens, the identified shear moduli converge towards the virtual work of the acceleration noise (equation 30) which happens to be very close to zero. Underestimation of material parameters due to low signal to noise ratio had already been mentioned for other inverse methods in [24].

  The relative error is thus lower than $\pm 2\%$ for good signal to noise ratio (close to the loading point) and reaches here -40% where the signal amplitude is small. Yet, the error of the maximal identified shear modulus $max(G', t)$ remains always better than -5%.
- The identified shear modulus G'_{app} obtained for the specific time $\omega t = 0$ (continuous black line) presents spatial oscillations as the signal to noise ratio changes with space. This result underlines that using a single frame would be insufficient to avoid identification artifacts.
- Finally, the best shear moduli G'_{best}, identified at time ωt when the virtual field amplitude $|\{q^{m*}_G\}|$ is minimal, are presented as diamonds. The best shear moduli present no longer identification artifacts. The identification error remains better than -2% for all considered signal to noise ratios. **One should thus use the shear modulus G'_{best}, identified when the virtual field amplitude $|\{q^{m*}_G\}|$ is minimal.**

These results underline the excellent identification abilities of the optimized virtual fields method, even when pressure waves are contained in the data.

Loss shear modulus G''_{app}: The relative error map $(\frac{G''_{app} - G''_{ref}}{G''_{ref}})$ of the loss shear modulus G''_{app} and its summary have been reported in Figure 7. The conclusions are mainly similar to the storage shear modulus G'_{app} but for the absence of identification bias and greater relative error. The greater relative error is due to the identical variance expression for the storage and loss shear moduli G' and G'' but different reference values G'_{ref} and G''_{ref} (Equation 51). The best identification is once more obtained when using the optimized virtual fields of minimal amplitude $|\{q^{m*}_G\}|$ with an error better than 25%.

Error origin: The error on the identified moduli has been previously expressed analytically. In both elastic and viscoelastic models, errors are due to the different virtual works of the noise (Elastic case, Equation 24, Viscoelastic case, Equation 67). As a reminder, the shear modulus error in the elastic case (Equation 24) can be written:

$$(G'_{app} - G') = \underbrace{-K'\ f_K(\underline{\underline{\epsilon}}^{no}, \underline{\underline{\epsilon}}^*_G)}_{\substack{\text{virtual work} \\ \text{of the bulk wave strain noise}}} \quad \underbrace{-G'\ f_G(\underline{\underline{\epsilon}}^{no}, \underline{\underline{\epsilon}}^*_G)}_{\substack{\text{virtual work} \\ \text{of the shear wave strain noise}}} + \underbrace{\int_{V_m} \rho\omega^2 \overrightarrow{u}^{no}.\overrightarrow{u}^*_G\, dV}_{\text{virtual work of the acceleration noise}} \tag{53}$$

Knowing the initial analytical signal and the added noise copy, the different parts of the error ($G'_{app} - G'_{ref}$) have been computed in the viscoelastic case (Figure 8). It appears that:

- The identification error is almost entirely due to the virtual work of the shear wave strain noise (Figure 8a and c).
- The virtual work of the bulk wave strain noise is almost equal to zero, which underlines the efficiency of the additional conditions to zero out the virtual work of the bulk wave strain noise.
- With the current simulation parameters (spatial subsampling, loading frequency), the virtual work of acceleration noise is negligible compared to the virtual work of the shear wave strain noise.

Bias and time dependence versus signal to noise ratio: Using the previous results, the bias and time dependences can be related to local signal to noise ratios. At each y positions, the signal to noise ratio $\gamma^{400}_{\epsilon_5}/|\epsilon_5|$ and $\gamma^{400}_{u}/|U_{Gx}|$ have been estimated: the standard deviation of the strain noise $\gamma^{400}_{\epsilon_5}$ and displacement noise γ^{400}_{u} are identical on the whole simulated data. The local shear wave amplitude of strain $|\epsilon_5|$ and displacement $|U_{Gx}|$ have been averaged over the mobile volume V_m.

The minimum, maximum and best local identified parameters have been computed from 50 noise copies. The averaged values over these 50 noise copies, referred to as $mean\big(\, min(G', t), N\big)$, $mean\big(\, max(G', t), N\big)$ and $mean\big(G'_{best}, N\big)$, have been presented in Figure 9. Two different noise levels $\gamma^{400}_{u} = 0.04\ \mu m$ and $0.4\ \mu m$ (respectively 0.2% (darker gray) and 2% (lighter gray) of the loading amplitude) have been studied to expand the analysis to lower signal to noise levels.

- The identification time dependence increases with the noise level. **This provides *a posteriori* information about the local signal to noise ratio time dependence.**
- The best identified shear moduli G'_{best} and G''_{best}, obtained with the optimized virtual fields requiring the minimal amplitude $|\{q^{m*}_G\}|$, underline the bias increase with the noise level. This phenomenon is due to the specialization conditions and will make the identified shear moduli G'_{best} and G''_{best} converge towards the virtual work of the acceleration noise, as explained in Section 2.3 (Equation 30), which is close to zero.
- When the signal to noise ratio $\gamma^{400}_{\epsilon_5}/|\epsilon_5|$ is as high as 37% (standard deviation), the storage shear modulus G'_{best} is identified with a relative error of only -10%. This underlines the excellent abilitiy of the optimized virtual fields method to identify mechanical parameters in noisy conditions, even if the strain is computed by discrete differentiation without any smoothing. If the noise level is too high to perform correct identification, the noise could be spatially smoothed using a Gaussian filter to lower the high frequency noise level before analyzig the data identification. Such a smoothing would yet add an additional bias to the identified parameters.

Virtual field richnesses: The previous identification results were obtained using a macro-element of 4*x4*x4* finite element functions, each finite element function containing 2x2x2 voxels (Table 3, line 1). These parameters strongly impact the identification robustness to noise:

- the number of free nodes (*i.e.* number of degree of freedom) directly impacts the OVFM ability to reach a virtual field minimizing the identified shear modulus population variance (equations 33, 39 and 45). Higher number of free node should allow better noise robustness.
- Yet, previous results show that a higher number of voxels per finite element function provides a better noise robustness than a high number of finite element function for fewer voxels [29].
- Eventually, the noise effect depends on the quantity of data in the mobile volume V_m. An increase of the size of the mobile volume V_m would improve the identification accuracy but would unfortunately also lower the identification spatial resolution.

The optimal parameter for the virtual field richness and size should thus be chosen so as to balance these different effects. These parameters depend on the data characteristics and desired identification spatial resolution.

Three different virtual field richness and size, presented in Table 3, have been tested on the analytical data. The minimum, maximum and best local identified parameters have been computed from 50 noise copies (noise levels $\gamma^{400}_{u} = 0.4\ \mu m$, *i.e.* 2% of the loading amplitude). The averaged values over these 50 noise copies have been presented in Figure 10.

- The previous identification results, obtained with the macro-element of 4*x4*x4* finite element functions and 8x8x8 voxels in V_m, are referred to as 1. (diamond markers) in Figure 10. For a signal to noise ratio $\gamma^{400}_{\epsilon_5}/|\epsilon_5|$ as high as 100% (relative standard deviation), the best identified storage and loss shear moduli G'_{best} and G''_{best} present errors of about 55% and 90%, respectively.
- The identification results obtained with the macro-element of 3*x3*x3* finite element functions and 9x9x9 voxels in V_m, labeled 2. (circle markers), present a better noise robustness than the macro-element 1. For a signal to noise ratio $\gamma^{400}_{\epsilon_5}/|\epsilon_5|$ as high as 100% (relative standard deviation), the best identified storage and loss shear moduli G'_{best} and G''_{best} present errors as low as 7% and 20%, respectively: the greater data volume (9x9x9 versus 8x8x8 voxels in V_m) and a lower spatial frequency of the virtual field (3x3x3 versus 2x2x2 voxels per finite element function) balance the diminution of free virtual nodes (8 versus 27 free virtual nodes in the macro-element).

  The identification time dependency of the macro-element 2. is unfortunately much greater than for the macro-element 1. and does not provide anymore *a posteriori* information about the local signal to noise ratio. The minimum identified storage shear modulus $min(G', t)$ is invariably close to zero: as explained in section 4.3, at specific times, the number of free virtual node is insufficient to provide both a special virtual field satisfying the required conditions and minimizing properly the noise impact; the identified shear modulus G' is erroneous at these times t. The best identified parameters with this macro-element G'_{best} and G''_{best} are still considered excellent considering the extreme noise level tested case.
- Eventually, the identification results obtained with the macro-element of 3*x3*x3* finite element functions and 6x6x6 voxels in V_m, labeled 3. (square markers), is presented. With these settings, the best identified storage and loss shear moduli G'_{best} and G''_{best} are as erroneous as 75% and 90%, respectively. Theses results are due to both small data volume V_m compared to the the shear wave wavelength λ_G and low virtual field richness.

5. Application

In this application section, virtual field richness of 4*x4*x4* finite element function and 8x8x8 voxels in V_m are used (Table 3, line 1). Now that the optimized virtual fields method is validated and understood, identification examples are presented on:

1. viscoelastic analytical waves using the hard boundary conditions in $y = 20\ mm$ and,
2. gel cube experimental data previously presented.

5.1. Viscoelastic analytical waves using the hard boundary conditions

As in the experimental data, a centered Gaussian noise of standard deviation $\gamma^{400}_u = 0.04\ \mu m$ (0.2% of the loading amplitude) is added to the analytical displacement field (Figure 11a). The only difference compared to the case previously presented (Figure 6 and 7) is the hard boundary condition for the shear wave at $y = 20\,mm$.

The results (Figure 11b and c) are globally similar to those of the soft boundary condition case (Figure 6c and 7c). The main differences are localized close to the boundary condition: the reflected wave creates local standing waves characterized by the presence of node and anti-nodes. At anti-node positions ($y = 16$ and $17.5\ mm$, horizontal lines in Figure 11), the signal to noise ratio is locally improved and the identification bias and time dependence decrease. On the contrary, at node positions ($y = 17$ and $18.5\ mm$), the displacement fields $\overrightarrow{u}$ and associated strain field $\underline{\underline{\epsilon}}$ amplitude are very small and/or badly extracted due to the virtual boundary conditions. The reflected shear wave thus increases the identification time dependence from -40% to -80% (compare Figure 6c and 7c with Figures 11b and c).

The best identified storage shear moduli G'_{best} are still within -10% of the reference storage shear moduli G'_{ref}, which is considered excellent. The loss shear modulus G''_{best} relative error is unfortunately greater and locally reaches $\pm 30\%$ of the reference value G''_{ref}.

5.2. Experimental data

The identification method is simply applied to the experimental data (Figures 1 and 2). The identification results are presented Figure 12.

As observed while analyzing the noisy simulations (Figure 6c and 7c), the time dependence of the identified parameters increases as the signal to noise ratio worsens. The best identified storage modulus G'_{best} also slightly decreases with the y position. As on the simulations, these results are attributed to the signal to noise ratio decrease

as the shear wave are damped by the material. It is yet considered that the identify storage and loss moduli G'_{best} and G''_{best} can be considered homogeneous on the cube and are respectively of about $1500 \pm 100\ Pa.$ and $250 \pm 50\ Pa.$

The differences between the experimental and simulated data are here attributed to difference between the chosen noise model and actual experimental noise.

6. Conclusion

In this work, the *optimized* virtual fields method has been further developed to analyze 3D dynamic displacement fields. The equations and method to identify elastic/viscoelastic models have been provided. The identification quality and method robustness to different parameters such as the spatial resolution and noise level have been studied. The study of error sources also provides guidance concerning proper analysis and estimation of material parameters. The following conclusions are valid for both elastic and viscoelastic models:

- while using linear virtual functions, the error induced by the experimental spatial resolution can been predicted and is independent from the identified model or number of voxels in the analyzed volume V_m.
- Analytical and numerical results underlined the bias induced by experimental noise onto the identified material parameters. The material parameters are usually underestimated; the bias increases non linearly when the signal to noise ratio deteriorates.
- The developed method rigorously deals with the presence of pressure waves in the data. Pressure waves thus do not affect the identification.
- The noise in the experimental data induces a time dependence of the identified parameters. Taking this time dependence into account provides error-bars giving *a posteriori* indications about the local signal to noise ratio.
- The best identification is obtained at a time ωt when the local optimized virtual fields has its smallest amplitude.
- The robustness to noise of the *optimized* virtual fields method is considered excellent. The procedure also yields some parameters indicating the robustness of the identification (η parameters). These can be used to provide *a posteriori* confidence intervals [33], at least when noise levels are low. Direct comparison between the different methods (noise sensitivity, spatial resolution and spatial contrast [24]) would need to be performed over different benchmark to quantify each method strengths and weaknesses. This will be an objective for futur work.

7. Recommendations

The following recommendations are proposed to users wishing to use the *optimized* virtual fields method for analysis of MRE data:

- The experimental settings (loading frequency, spatial sampling) should be chosen so as to provide at least 8 voxels par shear wavelength λ_G so that the relative error induced by the spatial sampling is lower than 5% (Figure 5). A spatial sampling better than 16 voxels par shear wavelength λ_G is recommended.
- With this method, the size of the mobile volume V_m should not be chosen smaller than half a shear wavelength. As the material parameters are assumed locally constant on this volume, the maximal identification spatial resolution is of the order of half a shear wavelength. This limitation should guide the experimental setting (loading frequency, spatial sampling) depending on the desired spatial resolution.
- A viscoelastic model should always be identified first from the data. This model provides good robustness to noise and only small biases due to low local signal to noise ratio.
- Due to the noise, the results obtained at a time ωt when the required local optimized virtual fields amplitude $|\{q_G^{m*}\}|$ is minimal should be considered as the more accurate identified values.

Acknowledgement

Funding was provided from NIH grant NS 055951 (Bayly) and from Arts et Metiers ParisTech, France.

Appendix

7.1. Development of the OVFM for viscoelastic models

For the sake of conciseness, the main equations required to implement the viscoelastic model are missing in the text body. These equations are provided in this appendix.

The viscoelastic model involves four parameters K', K'', G' and G'' (equation 12). As the principle of virtual work applied to the viscoelastic model provides a system of two equations (equation 15), two virtual fields would be required to estimate the four parameters. Yet, using the properties of *special* virtual fields, the shear storage and loss moduli G' and G'' have been identified using a unique *special* virtual field $\{\overrightarrow{u}^*_G, \underline{\underline{\epsilon}}^*_G\}$. The virtual field $\{\overrightarrow{u}^*_G, \underline{\underline{\epsilon}}^*_G\}$ is first injected into equation 15 which allows to write a two equation system:

$$\begin{bmatrix} \langle & f_K(\underline{\underline{\epsilon}}_\phi, \underline{\underline{\epsilon}}^*_G) & f_G(\underline{\underline{\epsilon}}_\phi, \underline{\underline{\epsilon}}^*_G) & f_K(\underline{\underline{\epsilon}}_{\phi+\frac{\pi}{2}}, \underline{\underline{\epsilon}}^*_G) & f_G(\underline{\underline{\epsilon}}_{\phi+\frac{\pi}{2}}, \underline{\underline{\epsilon}}^*_G) & \rangle \\ \langle & f_K(\underline{\underline{\epsilon}}_{\phi+\frac{\pi}{2}}, \underline{\underline{\epsilon}}^*_G) & f_G(\underline{\underline{\epsilon}}_{\phi+\frac{\pi}{2}}, \underline{\underline{\epsilon}}^*_G) & -f_K(\underline{\underline{\epsilon}}_\phi, \underline{\underline{\epsilon}}^*_G) & -f_G(\underline{\underline{\epsilon}}_\phi, \underline{\underline{\epsilon}}^*_G) & \rangle \end{bmatrix} \begin{bmatrix} K' \\ G' \\ K'' \\ G'' \end{bmatrix} = \begin{bmatrix} \int_{V_m} \rho\omega^2 \overrightarrow{u}_\phi . \overrightarrow{u}^*_G dV \\ \int_{V_m} \rho\omega^2 \overrightarrow{u}_{\phi+\frac{\pi}{2}} . \overrightarrow{u}^*_G dV \end{bmatrix} \tag{54}$$

The specialization conditions are written as:

$$f_K(\underline{\underline{\epsilon}}_\phi, \underline{\underline{\epsilon}}^*_G) = 0 \tag{55}$$

$$f_G(\underline{\underline{\epsilon}}_\phi, \underline{\underline{\epsilon}}^*_G) = 1 \tag{56}$$

$$f_K(\underline{\underline{\epsilon}}_{\phi+\frac{\pi}{2}}, \underline{\underline{\epsilon}}^*_G) = 0 \tag{57}$$

$$f_G(\underline{\underline{\epsilon}}_{\phi+\frac{\pi}{2}}, \underline{\underline{\epsilon}}^*_G) = 1 \tag{58}$$

With these specialization conditions, the equation system (equation 54) allows to compute the material parameters directly:

$$\begin{bmatrix} G' \\ G'' \end{bmatrix} = \frac{1}{2} \begin{bmatrix} \int_{V_m} \rho\omega^2 (\overrightarrow{u}_\phi + \overrightarrow{u}_{\phi+\frac{\pi}{2}}) . \overrightarrow{u}^*_G dV \\ \int_{V_m} \rho\omega^2 (\overrightarrow{u}_\phi - \overrightarrow{u}_{\phi+\frac{\pi}{2}}) . \overrightarrow{u}^*_G dV \end{bmatrix} \tag{59}$$

The errors in the material parameters can then be expressed by applying the system (equation 54) to noisy data, by injecting the specialization condition (equation 55) and simplifying it with the initial system applied to the noiseless signal (equation 54). To simplify the notation, the following contracted notation has been used:

$$f_{K(+\frac{\pi}{2})} = f_K(\underline{\underline{\epsilon}}^{no}_\phi + \underline{\underline{\epsilon}}^{no}_{\phi+\frac{\pi}{2}}, \underline{\underline{\epsilon}}^*_G) \tag{60}$$

$$f_{K(-\frac{\pi}{2})} = f_K(\underline{\underline{\epsilon}}^{no}_\phi - \underline{\underline{\epsilon}}^{no}_{\phi+\frac{\pi}{2}}, \underline{\underline{\epsilon}}^*_G) \tag{61}$$

$$f_{G(+\frac{\pi}{2})} = f_G(\underline{\underline{\epsilon}}^{no}_\phi + \underline{\underline{\epsilon}}^{no}_{\phi+\frac{\pi}{2}}, \underline{\underline{\epsilon}}^*_G) \tag{62}$$

$$f_{G(-\frac{\pi}{2})} = f_G(\underline{\underline{\epsilon}}^{no}_\phi - \underline{\underline{\epsilon}}^{no}_{\phi+\frac{\pi}{2}}, \underline{\underline{\epsilon}}^*_G) \tag{63}$$

$$f_{K(\frac{\pi}{2}-)} = f_K(\underline{\underline{\epsilon}}^{no}_{\phi+\frac{\pi}{2}} - \underline{\underline{\epsilon}}^{no}_\phi, \underline{\underline{\epsilon}}^*_G) \tag{64}$$

$$f_{G(\frac{\pi}{2}-)} = f_G(\underline{\underline{\epsilon}}^{no}_{\phi+\frac{\pi}{2}} - \underline{\underline{\epsilon}}^{no}_\phi, \underline{\underline{\epsilon}}^*_G) \tag{65}$$

With this notation, the error over each identified parameter is written:

$$\begin{bmatrix} G'_{app} - G' \\ G''_{app} - G'' \end{bmatrix} = -\frac{1}{2} \begin{bmatrix} \langle & f_{K(+\frac{\pi}{2})} & f_{G(+\frac{\pi}{2})} & f_{K(\frac{\pi}{2}-)} & f_{G(\frac{\pi}{2}-)} & \rangle \\ \langle & f_{K(-\frac{\pi}{2})} & f_{G(-\frac{\pi}{2})} & f_{K(+\frac{\pi}{2})} & f_{G(+\frac{\pi}{2})} & \rangle \end{bmatrix} \begin{bmatrix} K' \\ G' \\ K'' \\ G'' \end{bmatrix} + \frac{1}{2} \begin{bmatrix} \int_{V_m} \rho\omega^2 (\overrightarrow{u}^{no}_\phi + \overrightarrow{u}^{no}_{\phi+\frac{\pi}{2}}) . \overrightarrow{u}^*_G dV \\ \int_{V_m} \rho\omega^2 (\overrightarrow{u}^{no}_\phi - \overrightarrow{u}^{no}_{\phi+\frac{\pi}{2}}) . \overrightarrow{u}^*_G dV \end{bmatrix} \tag{66}$$

As an example, the error $(G'_{app} - G')$ can thus be written:

$$G'_{app} - G' = -\frac{1}{2} \left(\underbrace{K' f_K(\underline{\underline{\epsilon}}^{no}_\phi + \underline{\underline{\epsilon}}^{no}_{\phi+\frac{\pi}{2}}, \underline{\underline{\epsilon}}^*_G) + K'' f_K(\underline{\underline{\epsilon}}^{no}_{\phi+\frac{\pi}{2}} - \underline{\underline{\epsilon}}^{no}_\phi, \underline{\underline{\epsilon}}^*_G)}_{\text{virtual work of the bulk wave strain noise}} + \underbrace{G' f_G(\underline{\underline{\epsilon}}^{no}_\phi + \underline{\underline{\epsilon}}^{no}_{\phi+\frac{\pi}{2}}, \underline{\underline{\epsilon}}^*_G) + G'' f_G(\underline{\underline{\epsilon}}^{no}_{\phi+\frac{\pi}{2}} - \underline{\underline{\epsilon}}^{no}_\phi, \underline{\underline{\epsilon}}^*_G)}_{\text{virtual work of the shear wave strain noise}} \right) + \underbrace{\int_{V_m} \rho\omega^2 (\overrightarrow{u}^{no}_\phi + \overrightarrow{u}^{no}_{\phi+\frac{\pi}{2}}) . \overrightarrow{u}^*_G dV}_{\text{virtual work of the acceleration noise}} \tag{67}$$

As in the elastic case, a special attention is given to reduce the virtual work of the bulk wave strain noise, which can be reduced by additional conditions similar to the elastic case. The aim is to nullify the error coming from the virtual work of the bulk wave strain noise $K' f_K(\underline{\underline{\epsilon}}^{no}_{\phi} + \underline{\underline{\epsilon}}^{no}_{\phi+\frac{\pi}{2}}, \underline{\underline{\epsilon}}^{*}_{G})$ and $K'' f_K(\underline{\underline{\epsilon}}^{no}_{\phi+\frac{\pi}{2}} - \underline{\underline{\epsilon}}^{no}_{\phi}, \underline{\underline{\epsilon}}^{*}_{G})$. Using a similar reasoning as for the elastic case, this can be achieved by choosing a virtual field $\{\overrightarrow{u}^{*}_{G}, \underline{\underline{\epsilon}}^{*}_{G}\}$ so that $\int_{V_m} \rho\omega^2 \overrightarrow{u_{\phi K}}.\overrightarrow{u}^{*}_{G} dV = 0$ and $\int_{V_m} \rho\omega^2 \overrightarrow{u_{\phi+\frac{\pi}{2}K}}.\overrightarrow{u}^{*}_{G} dV = 0$. By assuming that *(i)* the bulk wavelength λ_K is much greater than the integration volum V_m and *(ii)* a constant material density ρ in V_m, these additional conditions are satisfied if:

$$\int_{V_m} u^{*}_{xG} dV = 0 \quad \text{and} \quad \int_{V_m} u^{*}_{yG} dV = 0 \quad \text{and} \quad \int_{V_m} u^{*}_{zG} dV = 0 \tag{68}$$

where u^{*}_{xG}, u^{*}_{yG}, and u^{*}_{zG} are the different component of the virtual displacement field $\overrightarrow{u}^{*}_{G}$.

One can then deduce that each parameter variance is written:

$$V(G'_{app}) = \frac{1}{4} \left[\begin{array}{cc} G' & G'' \end{array} \right] \left[V_{G'_{app}} \right] \left[\begin{array}{c} G' \\ G'' \end{array} \right] \tag{69}$$

$$V(G''_{app}) = \frac{1}{4} \left[\begin{array}{cc} G' & G'' \end{array} \right] \left[V_{G''_{app}} \right] \left[\begin{array}{c} G' \\ G'' \end{array} \right] \tag{70}$$

where

$$\left[V_{G'_{app}} \right] = \left[\begin{array}{cc} E((f_{G(+\frac{\pi}{2})})^2) & E(f_{G(\frac{\pi}{2}-)} f_{G(+\frac{\pi}{2})}) \\ s & E((f_{G(\frac{\pi}{2}-)})^2) \end{array} \right] \tag{71}$$

and

$$\left[V_{G''_{app}} \right] = \left[\begin{array}{cc} E((f_{G(-\frac{\pi}{2})})^2) & E(f_{G(+\frac{\pi}{2})} f_{G(-\frac{\pi}{2})}) \\ s & E((f_{G(+\frac{\pi}{2})})^2) \end{array} \right] \tag{72}$$

The values s indicate symmetrical values in the matrix and have not been reported to simplify the notation.

Using Wiener's integral properties and considering that the noise over $\underline{\underline{\epsilon}}^{no}_{\phi}$ and $\underline{\underline{\epsilon}}^{no}_{\phi+\frac{\pi}{2}}$ is not correlated and of the same amplitude ($\gamma_{\epsilon_\phi i} = \gamma_{\epsilon_{\phi+\frac{\pi}{2}} i}$), one can write:

$$\left[V_{G'_{app}} \right] = \left[V_{G''_{app}} \right] = 2 \left[\begin{array}{cc} E(f_G(\underline{\underline{\epsilon}}^{no}_{\phi}, \underline{\underline{\epsilon}}^{*}_{G})^2) & 0 \\ 0 & E(f_G(\underline{\underline{\epsilon}}^{no}_{\phi}, \underline{\underline{\epsilon}}^{*}_{G})^2) \end{array} \right] \tag{73}$$

where function $E(f_G^2)$ is identical to the function defined for the elastic material (equation 39).

Thus, the variance in G'_{app} and G''_{app} can then be simply written:

$$V(G'_{app}) = V(G''_{app}) = \frac{1}{2}(G'^2 + G''^2) E\big(f_G(\underline{\underline{\epsilon}}^{no}_{\phi}, \underline{\underline{\epsilon}}^{*}_{K})^2 \tag{74}$$

7.2. Analytical displacement field

The viscoelastic analytical wave solutions used in this work are shortly presented. Elastic materials can easily be simulated considering viscoelastic materials with no damping (bulk and loss moduli $K'' = \eta_K K'$ and $G'' = \eta_G G'$ equal to zero, equations 4 and 12).

Analytical solutions for viscoelastic shear and pressure waves can be found by solving the local equilibrium (equation 1) associated to the viscoelastic model (equation 12) and using appropriate initial and boundary conditions. The chosen analytical displacement simulates a shear and pressure wave combined: *(i)* a loading applied to the xz plane in the $\overrightarrow{x}$ direction to produce a plane shear wave traveling in the $\overrightarrow{y}$ direction and *(ii)* a plane pressure wave traveling in the $\overrightarrow{x}$ direction. The local displacement field is thus seen as the sum:

$$\overrightarrow{u} = (\underbrace{U_{rs} + U_{ls}}_{shear\,waves} + \underbrace{U_{rp} + U_{lp}}_{pressure\,waves})\overrightarrow{x} \tag{75}$$

where U_{rs} and U_{ls} are the shear waves propagating respectively in the right and left directions (respectively for increasing and decreasing y values). U_{rp} and U_{lp} are the pressure waves propagating respectively in the right and left direction.

The general expression of plane shear waves propagating in the right and left direction U_{rs} and U_{ls} are respectively:

$$U_{rs} = U_{rs0} \quad e^{-P_s y} \quad cos(\omega t - k_s y + \Phi_{rs}) \tag{76}$$

$$U_{ls} = U_{ls0} \quad e^{P_s y} \quad cos(\omega t + k_s y + \Phi_{ls}) \tag{77}$$

where U_{rs0} and U_{ls0} are the displacement amplitudes at $y = 0$. Φ_{rs} and Φ_{ls} are the wave phases. P_s and k_s are respectively the shear wave damping coefficient per unit of length and the spatial angular frequency such that:

$$P_s^2 = \frac{\rho\omega^2}{2} \frac{\sqrt{G'^2 + G''^2} - G'}{G'^2 + G''^2} \tag{78}$$

$$k_s^2 = \frac{\rho\omega^2}{2} \frac{\sqrt{G'^2 + G''^2} + G'}{G'^2 + G''^2} \tag{79}$$

The pressure wave equations are similar to the shear wave equations:

$$U_{rp} = U_{rp0} \quad e^{-P_p x} \quad cos(\omega t - k_p x + \Phi_{rp}) \tag{80}$$

$$U_{lp} = U_{lp0} \quad e^{P_p x} \quad cos(\omega t + k_p x + \Phi_{lp}) \tag{81}$$

P_p and k_p are respectively the pressure wave damping coefficient per unit of length and the spatial angular frequency. P_p and k_p can be simply obtained by replacing respectively G' and G'' by $K' + \frac{4G'}{3}$ and $K'' + \frac{4G''}{3}$ in equations 78 and 79.

The values U_{rs0}, U_{ls0}, Φ_{rs0}, Φ_{ls0} (respectively U_{rp0}, U_{lp0}, Φ_{rp0}, Φ_{lp0}) are chosen so as to respect the boundary conditions.

Different boundary conditions can be chosen, for example to simulate hard boundary conditions in $y = L$. The boundary conditions $\overrightarrow{u}(y = 0, t) = U_{x0} cos(\omega t)$ and $\overrightarrow{u}(y = L, t) = 0)$ lead to specific values of the parameters taking part in equation 76:

$$U_{ls0} = \frac{U_{x0} e^{-2P_s L}}{\sqrt{1 + e^{-4P_s L} - 2e^{(-2P_s L)} cos(2k_s L)}} \tag{82}$$

$$U_{rs0} = \frac{-U_{x0}}{\sqrt{1 + e^{-4P_s L} - 2e^{-2P_s L} cos(2k_s L)}} \tag{83}$$

$$\Phi_{rs} = \text{Atan}\left(\frac{sin(2k_s L)}{e^{-2P_s L} - cos(2k_s L)}\right) + 2k_s L \tag{84}$$

$$\Phi_{ls} = \text{Atan}\left(\frac{sin(2k_s L)}{e^{-2P_s L} - cos(2k_s L)}\right) \tag{85}$$

References

[1] S. Avril, M. Grédiac, F. Pierron, Sensitivity of the virtual fields method to noisy data, Computational Mechanics 34 (2004) 439–452.

[2] L. Gao, K. Parker, R. Lerner, S. Levinson, Imaging of the elastic properties of tissue - A review, Ultrasound in Medicine and Biology 22 (8) (1996) 959–977.

[3] J. Ophir, S. Alam, B. Garra, F. Kallel, E. Konofagou, T. Krouskop, T. Varghese, Elastography: ultrasonic estimation and imaging of the elastic properties of tissues, Proceedings of the Institution of Mechanical Engineers Part H- Journal of Engineering in Medicine 213 (H3) (1999) 203–233.

[4] P. Bayly, S. Ji, S. Song, R. Okamoto, P. Massouros, G. Genin, Measurement of strain in physical models of brain injury: a method based on harp analysis of tagged magnetic resonance images (MRI), Journal of Biomechanical Engineering 126 (2004) 523–528.

[5] P. Bayly, T. Cohen, E. Leister, D. Ajo, E. Leuthardt, G. Genin, Deformation of the human brain induced by mild acceleration, Journal of Neurotrauma 22 (2005) 84556.

[6] P. Bayly, E. Black, R. Pedersen, E. Leister, G. Genin, In vivo imaging of rapid deformation and strain in an animal model of traumatic brain injury, Journal of Biomechanics 39 (2006) 1086–95.

[7] K. McGee, D. Lake, Y. Mariappan, R. Hubmayr, A. Manduca, K. Ansell, R. L.Ehman, Calculation of shear stiffness in noise dominated magnetic resonance elastography data based on principal frequency estimation, Physics in Medicine and Biology 56 (14) (2011) 4291–4309.

[8] M. Yin, J. Woollard, X. Wang, V. Torres, P. Harris, C. J. Ward, K. J. Glaser, A. Manduca, R. Ehman, Quantitative assessment of hepatic fibrosis in an animal model with magnetic resonance elastography, Magnetic Resonance in Medicine 58 (2) (2007) 346–353.

[9] S. Venkatesh, M. Yin, J. Glockner, N. Takahashi, P. Araoz, J. Talwalkar, R. L.Ehman, MR elastography of liver tumors: Preliminary results, American Journal of Roentgenology 190 (6) (2008) 1534–1540.

[10] S. Bensamoun, S. Ringleb, L. Littrell, Q. Chen, M. Brennan, R. Ehman, K. An, Determination of thigh muscle stiffness using magnetic resonance elastography, Journal of Magnetic Resonance Imaging 23 (2) (2006) 242–247.

[11] J. Zhang, M. Green, R. Sinkus, L. Bilston, Viscoelastic properties of human cerebellum using magnetic resonance elastography, Journal of Biomechanics 44 (10) (2011) 1909–1913.

[12] I. Sack, B. Beierbach, U. Hamhaber, D. Klatt, J. Braun, Non-invasive measurement of brain viscoelasticity using magnetic resonance elastography, NMR in Biomedicine 21 (3) (2008) 265–271.

[13] M. Green, L. Bilston, R. Sinkus, In vivo brain viscoelastic properties measured by magnetic resonance elastography, NMR in Biomedicine 21 (7) (2008) 755–764.

[14] S. Kruse, G. Rose, K. Glaser, A. Manduca, J. Felmlee, R. J. Clifford, R. Ehman, Magnetic resonance elastography of the brain, NeuroImage 39 (1) (2008) 231–237.

[15] R. Sinkus, M. Tanter, S. Catheline, J. Lorenzen, C. Kuhl, E. Sondermann, M. Fink, Imaging anisotropic and viscous properties of breast tissue by magnetic resonance-elastography, Magnetic Resonance in Medicine 53 (2) (2005) 372–387.

[16] S. Avril, P. Badel, A. Duprey, Anisotropic and hyperelastic identification of in vitro human arteries from full-field optical measurements, Journal of Biomechanics 43 (2010) 2978–2985.

[17] F. Hendriks, D. Brokken, J. Van Emeren, C. Oomens, F. Baaijens, J. Horsten, A numerical-experimental method to characterize the non-linear mechanical behavior of human skin, Skin Research and Technology 9 (3) (2003) 274–283.

[18] J. Schmitt, OCT elastography: imaging microscopic deformation and strain of tissue, Optics Express 3 (6) (1998) 199–211.

[19] T. Oida, A. Amano, T. Matsuda, Magnetic resonance elastography: in vivo measurements of elasticity for human tissue, in: Informatics Research for Development of Knowledge Society Infrastructure, 2004. ICKS 2004. International Conference on, 2004, pp. 57–64.

[20] R. Muthupillai, D. Lomas, P. Rossman, J. Greenleaf, A. Manduca, R. Ehman, Magnetic resonance elastography by direct visualization of propagating acoustic strain waves, Science 269 (5232) (1995) 1854–1857.

[21] A. Baghani, S. Salcudean, R. Rohling, Theoretical limitations of the elastic wave equation inversion for tissue elastography, The Journal of the Acoustical Society of America 126 (3) (2009) 1541–1551.
URL `http://link.aip.org/link/?JAS/126/1541/1`

[22] S. Avril, M. Bonnet, A. S. Bretelle, M. Grédiac, F. Hild, P. Ienny, F. Latourte, D. Lemosse, S. Pagano, E. Pagnacco, F. Pierron, Overview of identification methods of mechanical parameters based on full-field measurements, Experimental Mechanics 48 (4) (2008) 381–402.

[23] J. Smith, R. Ehman, Extraction of propagating waves in cine images from magnetic resonance elastography, Materials Evaluation 58 (12) (2000) 1395–1401.

[24] A. Manduca, T. Oliphant, M. Dresner, J. Mahowald, S. A. Kruse, E. Amromin, J. P. Felmlee, J. F. Greenleaf, R. L. Ehman, Magnetic resonance elastography: Non-invasive mapping of tissue elasticity, Medical Image Analysis 5 (4) (2001) 237–254.

[25] A. Romano, J. Bucaro, R. Ehnan, J. Shirron, Evaluation of a material parameter extraction algorithm using MRI-based displacement measurements, Ultrasonics, Ferroelectrics and Frequency Control, IEEE Transactions on 47 (6) (2000) 1575–1581.

[26] F. Pierron, P. Bayly, R. Namani, Application of the virtual fields method to magnetic resonance elastography data, Proceedings of the 2010 SEM Annual Conference and Exposition on Experimental and Applied Mechanics 1 (681-688).

[27] S. Avril, J. M. Huntley, F. Pierron, D. D. Steele, 3D heterogeneous stiffness reconstruction using MRI and the virtual fields method, Experimental Mechanics 48 (4) (2008) 479–494.

[28] A. Giraudeau, F. Pierron, Identification of stiffness and damping properties of thin isotropic vibrating plates using the virtual fields method: theory and simulations, Journal of Sound and Vibration 284 (3-5) (2005) 757–781.

[29] F. Pierron, M. Grédiac, The Virtual Fields Method: Extracting constitutive mechanical parameters from full-field deformation measurements, Springer New-York, 2012.

[30] T. Soong, M. Grigoriu, Random vibration of mechanical and structural systems, PTR Prentice Hall, Inc, 1993.

[31] E. Toussaint, M. Grédiac, F. Pierron, The virtual fields method with piecewise virtual fields, International Journal of Mechanical Sciences 48 (3) (2006) 256–264.

[32] A. Giraudeau, F. Pierron, B. Guo, An alternative to modal analysis for material stiffness and damping identification from vibrating plates, Journal of Sound and Vibration 329 (10) (2010) 1653–1672.

[33] F. Pierron, G. Vert, R. Burguete, S. Avril, R. Rotinat, M. R. Wisnom, Identification of the orthotropic elastic stiffnesses of composites with the virtual fields method: Sensitivity study and experimental validation, Strain 43 (3) (2007) 250–259.

Viscoelastic material:	$E = 4.7$ kPa	$\nu = 0.49$	$\eta = 0.15$	$\rho = 1000\ kg.m^{-3}$
Associated parameters:	$G' = 1577$ Pa $K' = 78.3$ kPa	$G'' = 236$ Pa $K'' = 11.7$ kPa	$\lambda_G(400Hz) = 3.2$ mm $\lambda_K(400Hz) = 22.6$ mm	

Table 1: Parameters for the simulated elastic or viscoelastic material

Cube length:	– $L = 30$ mm
Loading frequency:	– $f = 400$ Hz
Shear wave traveling along $\overrightarrow{z}$ • Hard BC: • Soft BC:	– $U_{Sx}(z = 0) = 20\ \mu m$ – $U_{Sx}(z = L) = 0\ \mu m$ – No condition on $U_{Sx}(z = L)$
Pressure wave traveling along $\overrightarrow{x}$ • Soft BC:	– $U_{Kx}(x = 0) = 1\ \mu m$ – No condition on $U_{Kx}(x = L)$
Temporal resolution: Spatial resolution:	– 8 pictures per cycle – 16 voxels per λ_G

Table 2: Loading, geometrical and resolution parameters

Designation number	Number of virtual elements	Size of mobile volume V_m (voxels^3)
1.	4*x4*x4* (27 free nodes)	8x8x8 (2x2x2 voxels^3 per FE function
2.	3*x3*x3* (8 free nodes)	9x9x9 (3x3x3 voxels^3 per FE function)
3.	3*x3*x3* (8 free nodes)	6x6x6 (2x2x2 voxels^3 per FE function)

Table 3: Virtual field richnesses and sizes

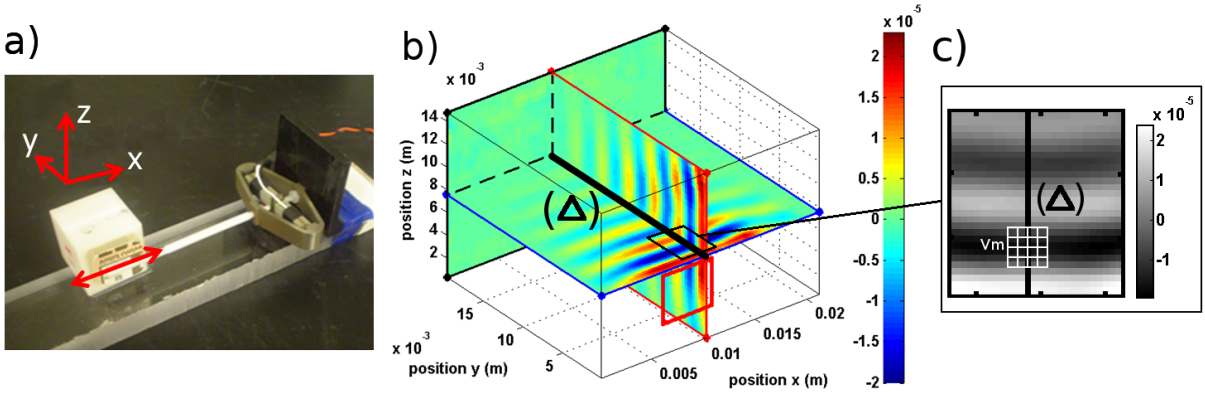

Figure 1: a) Experimental setup, b) Raw displacement results U_x^{400} and line (Δ), c) Zoom-in and macro-element of volume V_m.

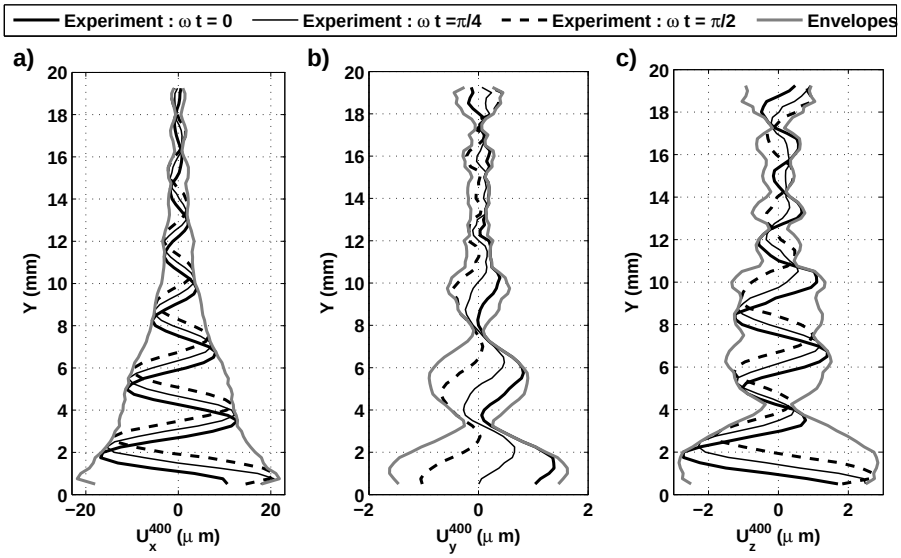

Figure 2: Experimental data: displacements U_x^{400}, U_y^{400} and U_z^{400} along a line in the cubic sample. Note: scale in subfigures b) and c) are expanded.

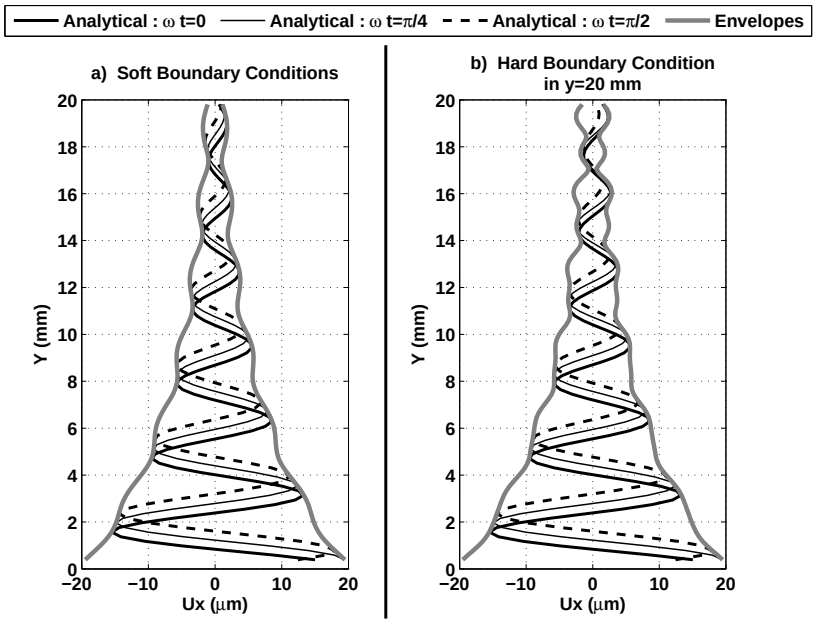

Figure 3: Example of analytical data: a) Soft boundary condition, b) Hard boundary condition for the shear wave in $y = 20\ mm$.

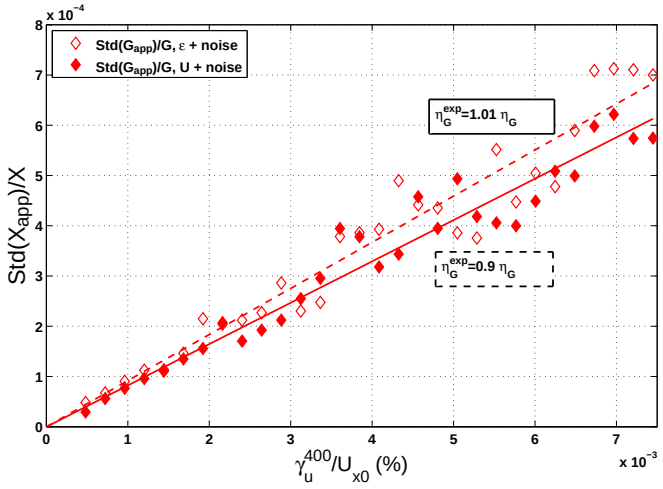

Figure 4: Standard deviation of the identified parameters K'_{app} and G'_{app} identified for several standard deviation values of the input noise γ_u^{400} (method proposed in [1]).

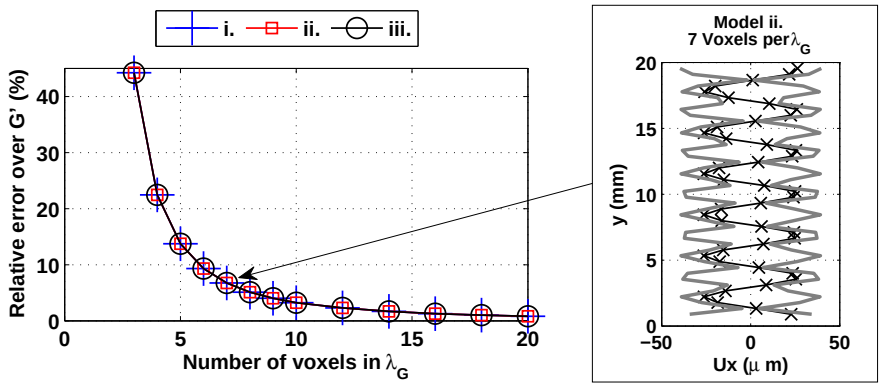

Figure 5: Relative error on G' for different spatial resolutions.

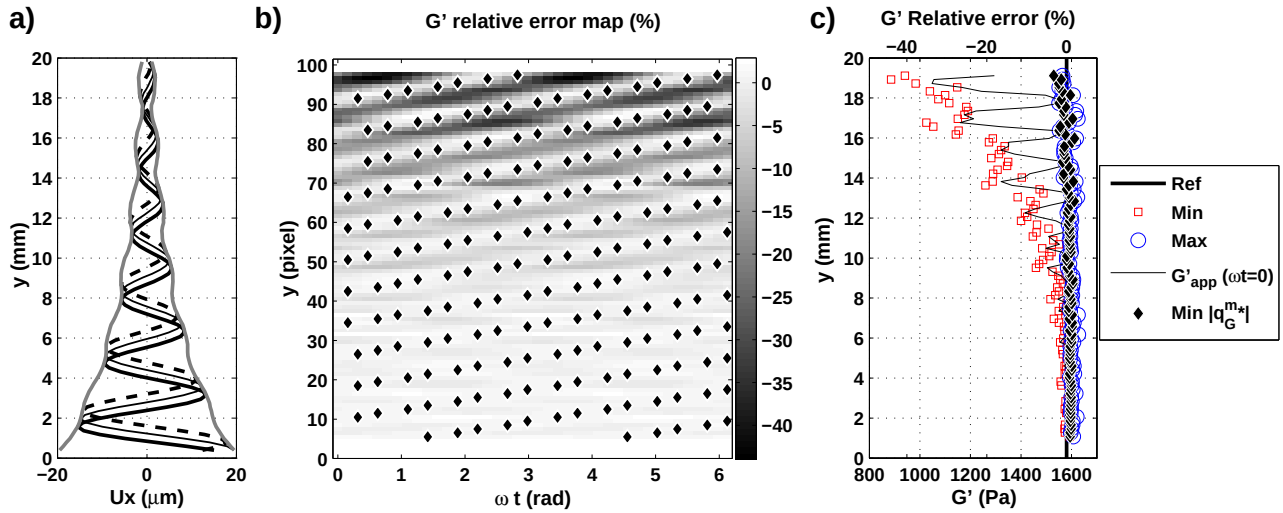

Figure 6: Identification results for the viscoelastic model. a) Noisy input displacement field ($\gamma_u^{400} = 0.04\ \mu m$, soft boundary conditions), (b) identified G' space-time error map and (c) associated summary

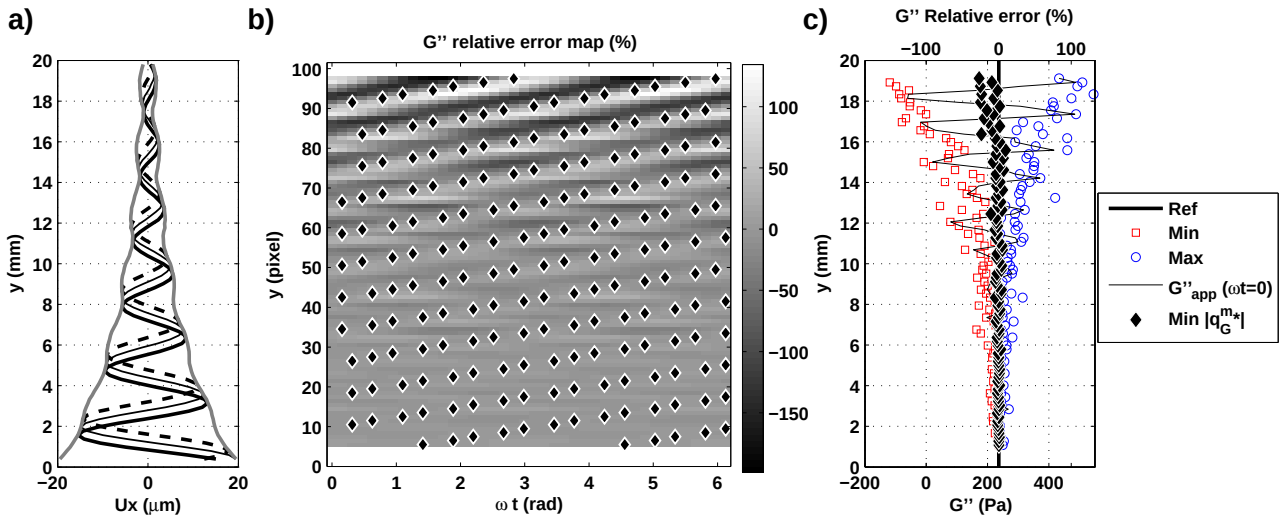

Figure 7: Identification results for the viscoelastic model. a) Noisy input displacement field ($\gamma_u^{400} = 0.04\ \mu m$, soft boundary conditions), (b) identified G'' space-time error map and (c) associated summary

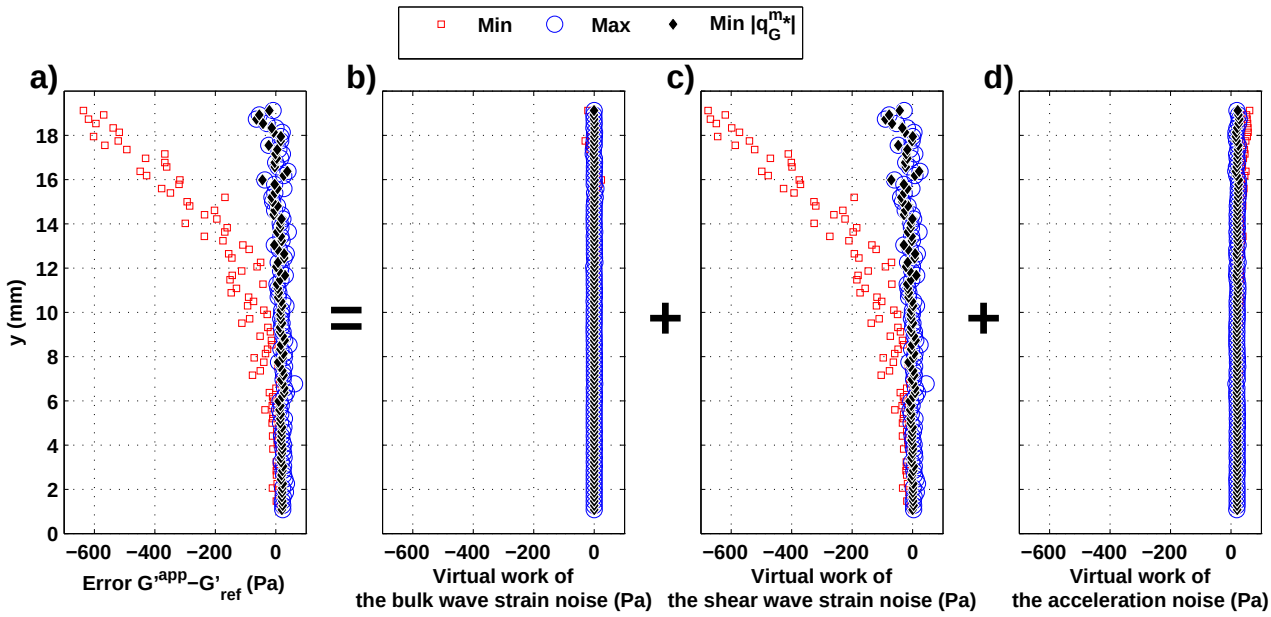

Figure 8: G' error origin while identifying an viscoelastic model from noisy viscoelastic pressure and shear waves. (a) Error: $G' - G'_{ref} =$ (b) virtual work of the bulk wave strain noise + (c) virtual work of the shear wave strain noise + (d) virtual work of the acceleration noise.

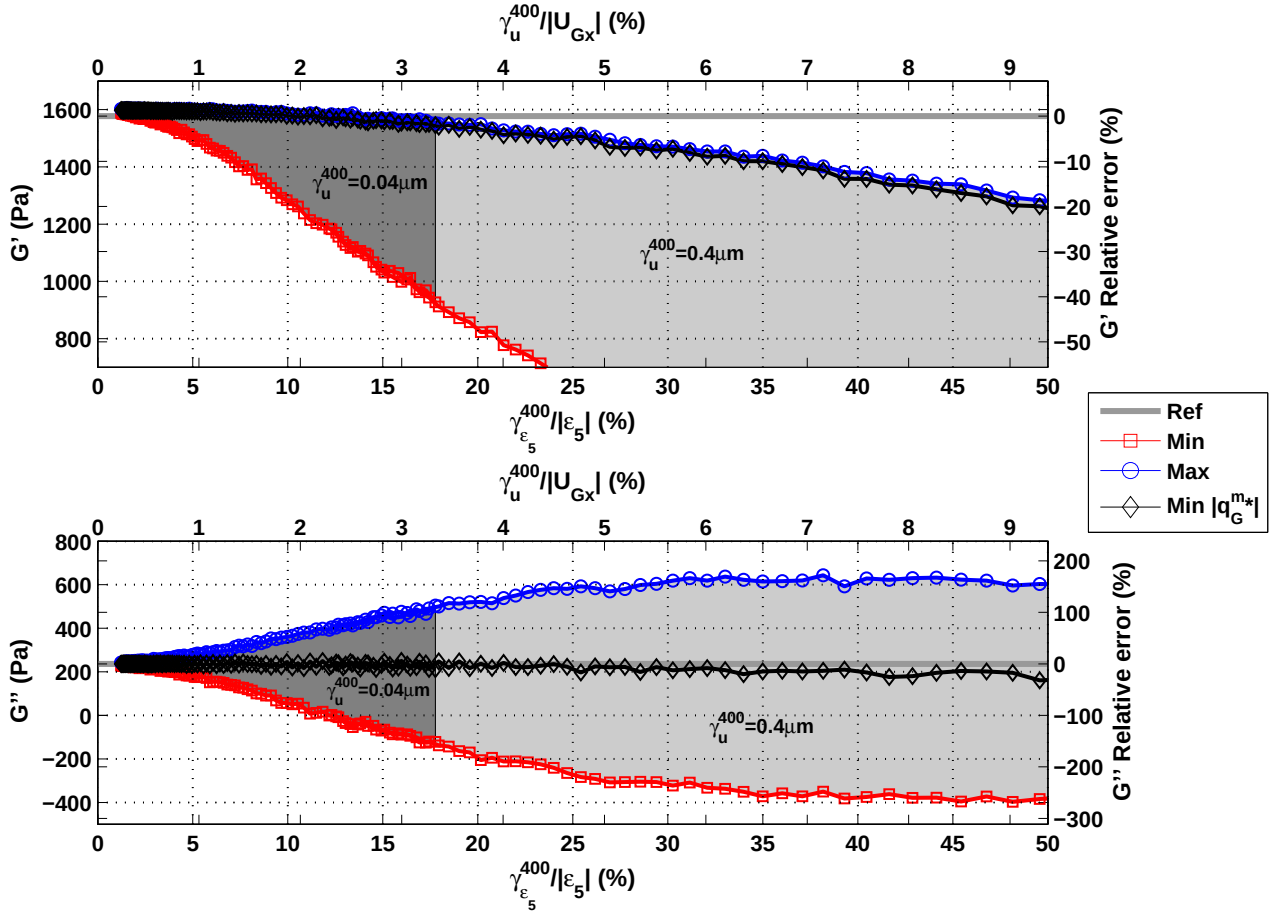

Figure 9: Maximum, minimum and best identified values over time versus noise level for 50 different noise copies on viscoelastic waves. Upper graph: G' Bottom graph: G''

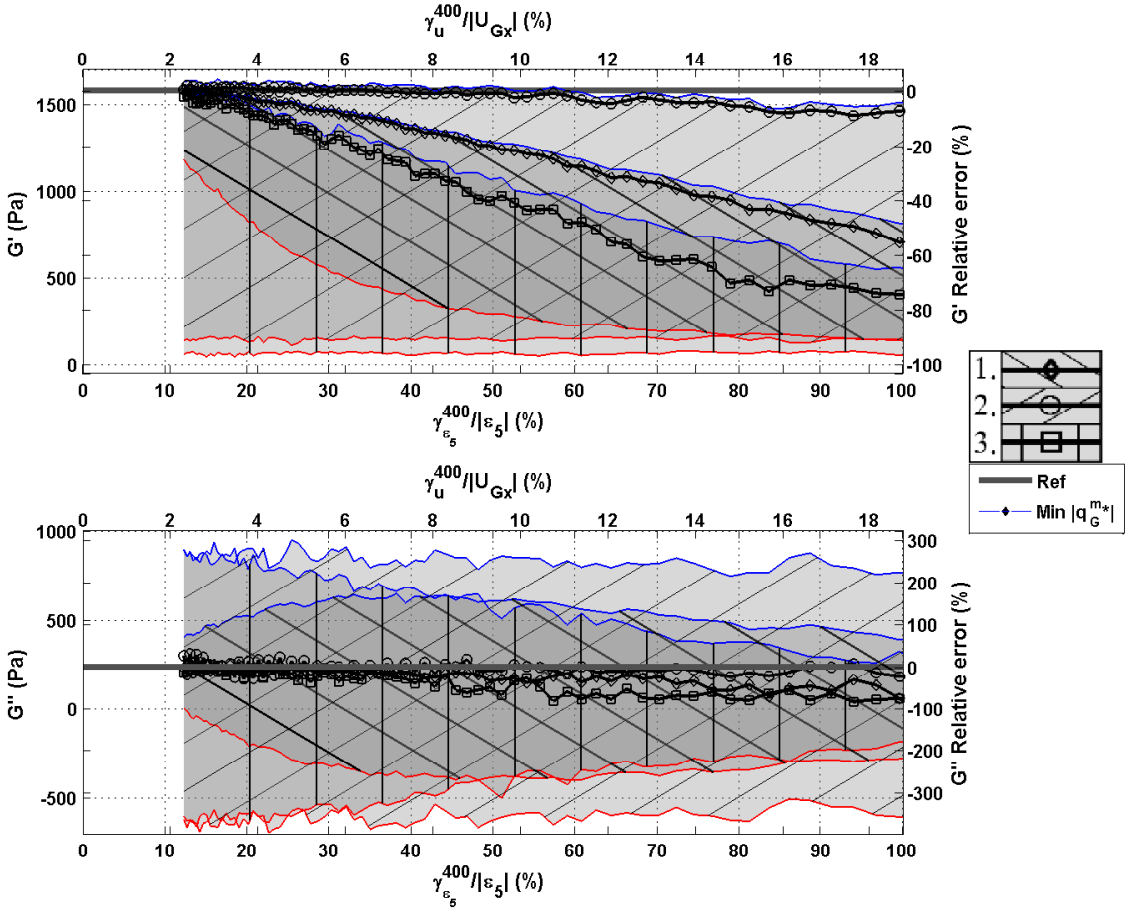

Figure 10: Identification results for the viscoelastic model for different virtual field size and richness (Table 3). Averaged values on 50 different noise copies.

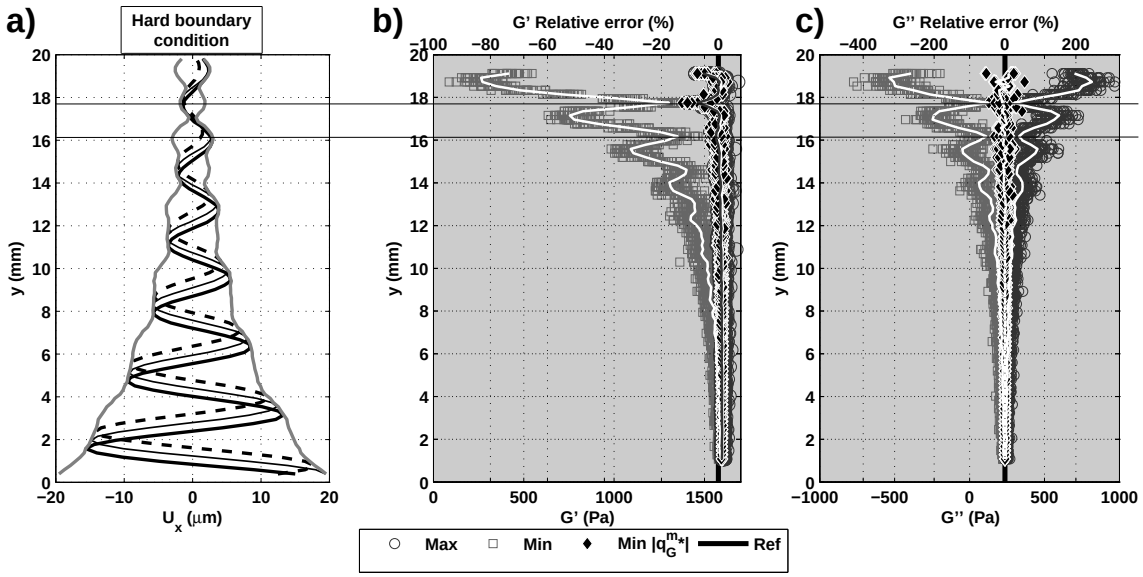

Figure 11: Identification results for the viscoelastic model for 25 different noise copies. a) Noisy input displacement field ($\gamma_u^{400} = 0.04\ \mu m$, hard boundary conditions), b) Storage shear modulus G', (c) Loss shear modulus G''.

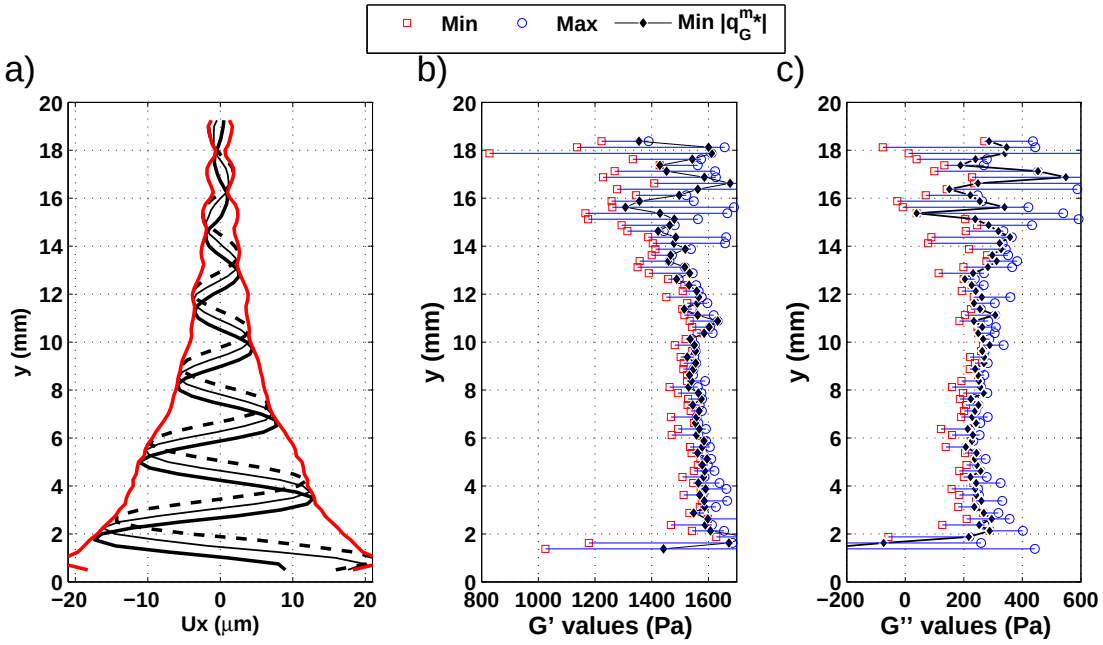

Figure 12: Identification results on experimental data. a) Input displacement field, b) Storage shear modulus G', (c) Loss shear modulus G''.